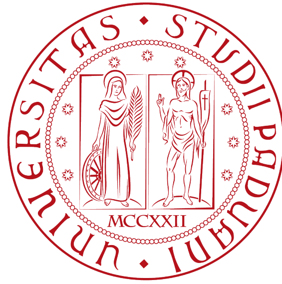

UNIVERSITÀ DEGLI STUDI DI PADOVA

Dipartimento di Fisica e Astronomia "Galileo Galilei"

Master Degree in Astrophysics and Cosmology

Final Dissertation

Experimental investigation of stray light from dust contamination in gravitational wave detectors

Thesis supervisor:

Prof. Giacomo Ciani

Thesis co-supervisor:

Dr. Livia Conti

Candidate:

Francesco Flocco

Academic Year 2023/2024

Abstract

Stray light presents a significant challenge in the LIGO-Virgo interferometers, manifesting as excess noise in the low-frequency region and causing a loss in sensitivity both through increased measurement noise and disruption of control loops. This issue is expected to be even more critical in future interferometers, such as the Einstein Telescope (ET), which will have higher sensitivity in the low-frequency region. Therefore, effective monitoring and mitigation of stray light sources are crucial.

This thesis focuses on understanding and controlling stray light contributions, primarily from surface roughness and dust particles deposited on optical components. The Bidirectional Scattering Distribution Function (BSDF) and Total Integrated Scattering (TIS) are utilized to model and characterize stray light sources. The Harvey-Shack model and its generalized form, along with Mie scattering theory, are applied to understand the scattering phenomena.

The research included significant enhancements to a scattering measurement facility, including background noise optimization and the implementation of automated measurement procedures. Various samples, including baffle components from Virgo detectors, absorbent glass samples, and silicon wafers used in dust monitoring campaigns, were characterized using the improved facility for their scattering properties.

The facility's future focus will be on supporting the dust monitoring campaign, with new wafers periodically exposed in various environments of the Virgo laboratories to monitor dust accumulation. These measurements will help validate BSDF estimates and improve the overall understanding of stray light contributions in gravitational wave detectors.

Contents

1 Introduction **1**
1.1 Gravitational Waves 1
1.2 Gravitational wave astronomy 4
1.3 The issue of straylight 11

2 Straylight **15**
2.1 Basic Radiometry 15
2.2 Scattering from Roughness 19
2.2.1 Roughness model 19
2.2.2 Scattering model - Harvey-Shack 21
2.2.3 Generalized Harvey-Shack Model 23
2.3 Scattering from Particulate 27

3 Scattering measurement facility **31**
3.1 Optical Setup 31
3.1.1 Scatterometer 33
3.1.2 Integrating Sphere 38
3.2 Current State and Facility Upgrades 39
3.2.1 Pickup Detector 40
3.3 Scatterometer Background 43
3.3.1 Theoretical noise floor for BRDF measurements 43
3.3.2 Scatterometer Background Optimization 47

4 Measurements **53**
4.1 Scattering from surface roughness 54
4.1.1 Effective RMS Roughness 54
4.1.2 CERN steel samples 55
4.1.3 Baffles samples 57
4.1.4 Absorbent glass samples 59
4.1.5 Clean Silicon wafer 61
4.2 Dust scattering measurements 64
4.2.1 Wafer contaminated by Ti calibrated dust 65

5 Conclusion **69**

Chapter 1

Introduction

1.1 Gravitational Waves

Formulated over a century ago, Einstein's theory of General Relativity fundamentally altered our understanding of gravity, representing it not as a instantaneous force among massive objects, like Newtonian physics, but as the result of curvature of the spacetime. In the theory of General Relativity, spacetime is not just a passive background for the events of the universe; rather, its curvature change in response to the presence of mass and energy. Objects with mass influence this curvature, causing free masses to move according to this curvature, moving through paths that minimize the spacetime interval, known as geodesics. To external observers, this motion appears as acceleration.

Under certain conditions of motion, such as asymmetric accelerations, masses can induce fluctuations in the curvature of spacetime, giving rise to gravitational waves (GWs hereafter). These waves travel at the speed of light, carrying energy and angular momentum. They are transverse, meaning they distort spacetime in a plane perpendicular to their direction of propagation, and traceless, indicating that their effects on two orthogonal directions within this plane are opposite. Observing a GW far from its source of generation, when it encounters objects in its path, it causes a stretching effect on these objects. Consequently, the amplitude of GWs is typically quantified with "strain", representing the fractional change in length experienced by objects as the waves pass through them, providing a measurable signal that can be detected by sensitive instruments here on Earth.

GW emission The process governing the emission of GWs is encapsulated within the *quadrupole formula*. This formula arises from solving Einstein's equations under the approximation of "linearised gravity" and considering small perturbations of the metric. As for a fully detailed discussion of General Relativity, the complete derivation of GW waveform parameters is out of the scope of this thesis and can be found in [1]. However, it is possible to approximate the leading form of the GW field using straightforward physical arguments and dimensional analysis, linking the strain generated to the moment of the mass.

Following ref. [2], let us consider a system with an isolated source at a distance r from an observer. By adopting an approximation that considers a slowly moving,

weakly self-gravitating source, the goal is to derive a dimensionless strain, denoted as h, which exhibits radiative behavior and diminishes proportionally to $1/r$. This approximation uses only the gravitational constant G and the speed of light c as restoring factors.

The derivation begins by defining some moments of the mass distribution. The zeroth moment M_0 is just the total mass-energy of the source:

$$M_0 \equiv \int \rho \, d^3x = M \tag{1.1}$$

Where ρ is the mass density.

Then we define the dipole moment M_1:

$$M_{1i} \equiv \int \rho \, x_i \, d^3x = ML_i \tag{1.2}$$

The vector L_i has the dimensions of length and represents the displacement of the center of mass from the origin. We can see, that the parameter M_1 is not a very meaningful quantity, as its value change simply by choosing a different origin.

Considering the possibility of internal motion within our mass distribution, the moments of the mass current, denoted as $j_i = \rho v_i$, become significant. The first moment corresponds to the spin angular momentum:

$$S_1 \equiv \int \rho \, v_j \, x_k \, \epsilon_{ijk} \, d^3x = S_i \tag{1.3}$$

Finally, we look at the second moment of the mass distribution:

$$M_2 \equiv \int \rho \, x_i \, x_j \, d^3x = ML_{ij} \tag{1.4}$$

where L_{ij} is a tensor with the dimension length squared. Let's start by considering M_0. We aim to combine M_0 with the distance to our source, r, in a manner that yields a dimensionless wave strain h. The only viable way to achieve this is:

$$h \sim \frac{G}{c^2} \frac{M_0}{r} \tag{1.5}$$

This formula doesn't make sense for radiation. Conservation of mass-energy imposes that M_0 for an isolated source is constant. Consequently, this h cannot exhibit radiative behavior; it corresponds to a Newtonian potential rather than a GW.

Continuing with the moment M_1, To ensure dimensional consistency, we must take one time derivative:

$$h \sim \frac{G}{c^3} \frac{d}{dt} \frac{M_1}{r} \tag{1.6}$$

However, about the derivative of M_1:

$$\frac{dM_1}{dt} = \frac{d}{dt} \int \rho x_i \, d^3x = \int \rho v_i \, d^3x = P_i \tag{1.7}$$

This cannot describe a GW because of conservation of momentum: the momentum of an isolated source must remain conserved. Through a Lorentz boost into a different frame, we can always nullify $P = 0$. Terms such as these are typically gauge artifacts, they do not correspond to radiation.

Continuing with S_1, dimensional analysis imposes that radiation from spin momentum must show as:

$$h \sim \frac{G}{c^4}\frac{d}{dt}\frac{S_1}{r} \tag{1.8}$$

The conservation of angular momentum affirms that the total spin of an isolated system remains constant. Therefore, we reject this term for the same reasoning we neglected equation 1.5, it cannot correspond to radiation.

Lastly, let's analyse M_2:

$$h \sim \frac{G}{c^4}\frac{d^2}{dt^2}\frac{M_2}{r} \tag{1.9}$$

There isn't a conservation principle that forces us to discard this term. This term encapsulates the leading form of the quadrupole formula, differing from the formally derived result by numerical factors.

In 'normal' units, the prefactor of this formula translates to G/c^4, resulting in a very small factor. To generate significant GWs, the quadrupole moment's variation must be substantial. Only sources with exceptionally large masses undergoing extremely rapid variations will yield significant GWs; even then, the expected strain from typical sources is minuscule. As a consequence, it is extremely unlikely there will ever be an interesting laboratory source of GWs. Only astrophysical objects that are sufficiently massive and relativistic have the potential to generate detectable gravitational waves, in spite of their much larger distance with respect to a source on the Earth.

Therefore, for a system with a given mass distribution and temporal evolution using the leading form of the quadrupole formula, it is possible to predict the emission of GWs in terms of frequency and phase. For that, astrophysical sources can be naturally classified into four distinct classes based on the type of GW signal they emit [3].

The first class consists of burst sources, including the formation of neutron stars and black holes in supernova events. The burst signal generated by these events typically comprises a very short single event.

The second class comprises narrow-band sources, encompassing phenomena like the rotation of single non-axisymmetric stars, notably pulsars and accreting neutron stars. Typically, these sources are weaker compared to burst sources.

The third category consists of compact binary inspiral sources. These systems are composed of two compact objects orbiting each other. Over time, as the system emits gravitational waves, it loses energy, causing the objects to spiral inwards and move closer together until they eventually merge. The emitted signal can be divided into two phases: an initial quasi-periodic phase where the system is distant from coalescence, exhibiting period evolution due to gravitational wave energy loss, and a final coalescence phase. The final phase consists of a strong but short signal comprising the last cycles of the binary, culminating in the merger of the objects.

These binary coalescence events may involve binary neutron stars, binary black holes, or neutron-star–black-hole binaries.

The last category of sources includes stochastic backgrounds generated by the integrated effects of numerous weak periodic sources within our Galaxy, or from a vast population of burst sources at significant distances, along with cosmological processes in the early universe. Detecting stochastic backgrounds poses a challenge in single detectors as they are virtually indistinguishable from instrument noise.

1.2 Gravitational wave astronomy

The weak interaction of GWs is both a blessing and a curse: on one hand, it allows them to propagate from emission to Earth-bound observers with minimal absorption, enabling the exploration of astrophysical phenomena hidden or obscured from electromagnetic observations, such as the coalescence and merger of black holes, the collapse of stellar cores, and the dynamics of the early Universe. On the other hand, their weak interaction makes GW detection extremely challenging. Moreover, since many of the most promising GW sources are hidden or obscured, our understanding of them remains limited, we have limited knowledge about what is likely to be some of the most significant sources of GWs.

Like electromagnetic waves, gravitational waves also admit two polarizations and are transverse to the direction of propagation (+ and $\times$). Let's examine a ring of test masses positioned on the xy plane with a sinusoidal GW propagating along the z-axis. The relative acceleration of the test masses remains within the xy plane. In the case of a + polarized wave, it alternately elongates distances along the x-axis while simultaneously compressing them along the y-axis. Half a period later, it contracts distances along the x-axis while simultaneously elongating them along the y-axis. The same pattern is repeated for the cross-polarization but is rotated by 45° in the xy plane. Figure 1.1 illustrates the visual impact of a GW passage for both polarizations on the xy plane of a perpendicular wave (z-axis).

The distortion of spacetime resulting from the passage of a GW cannot be directly measured by placing equally spaced points (namely a ruler) along it, as they would undergo identical stretch or compression. However, light maintains a constant speed c. Therefore, if the space between two objects stretches, light would take longer to traverse the distance between them, and if the space compresses, light would take less time to cover the same distance. Specifically, the distortion of spacetime caused by a passing GW cannot be measured directly using a single point, as a single point can always be described in an inertial reference frame where it is in free fall. To detect GWs, at least two points (or particles) are needed to measure the relative change in distance between them.

Detectors This is where interferometers (ITF) come into play. Interferometers are devices that utilize lasers and interferometry to gauge the alteration in distance between two reference points induced by gravitational waves. Among the most significant GW detectors currently in operation are the second-generation interferometric detectors: Advanced LIGO (aLIGO) in the US, and Advanced Virgo (AdVirgo) in

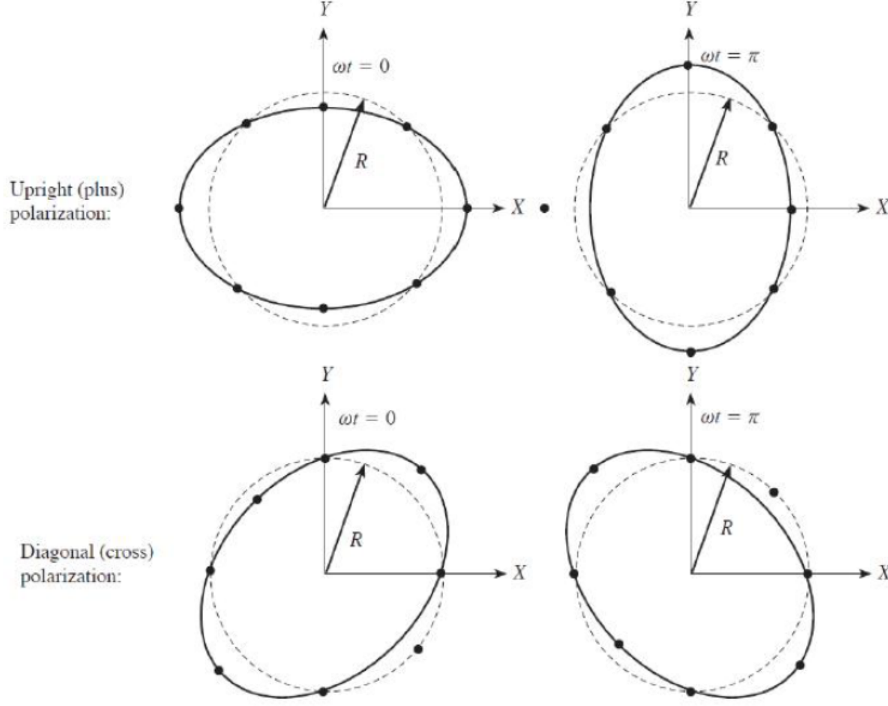

Figure 1.1: Effect of a GW propagating along the z-axis for a ring of test masses placed on the (x,y) plane.

Italy. These detectors are based on the principles of a Michelson interferometer but are more complex and very large to achieve greater sensitivities.

Current advanced detectors consist of two arms constructed perpendicular to each other. In the case of aLIGO, these arms extend 4 kilometers in length, while those of AdVirgo are 3 kilometers. Positioned at the intersection between the two arms is a beam splitter. A laser beam is directed towards the beam splitter, where it divides into two beams of equal power, each traveling along one of the arms. At the end of each arm, the beams are reflected by mirrors, serving as the test masses, and subsequently recombine upon returning to the beam splitter, thereby interfering with each other.

The interference between the two beams is correlated with the difference in the path length they traverse. This difference is adjusted to achieve nearly complete destructive interference at the output in the absence of GWs. However, it changes when a passing wave distorts the arms and displaces the test masses. The orthogonal alignment of the two arms matches the fact that GWs impact oppositely in two orthogonal directions, thereby optimizing the alteration in the interference pattern. Consequently, we can measure and quantify the strain induced by the GW on the arms.

In the real world, the positions of the mirrors are influenced by noise from various sources. Therefore, understanding the origins of these noises is crucial to minimize their impact on the interferometer. Different strategies have been employed to mitigate these noises in existing advanced detectors, and additional methods will

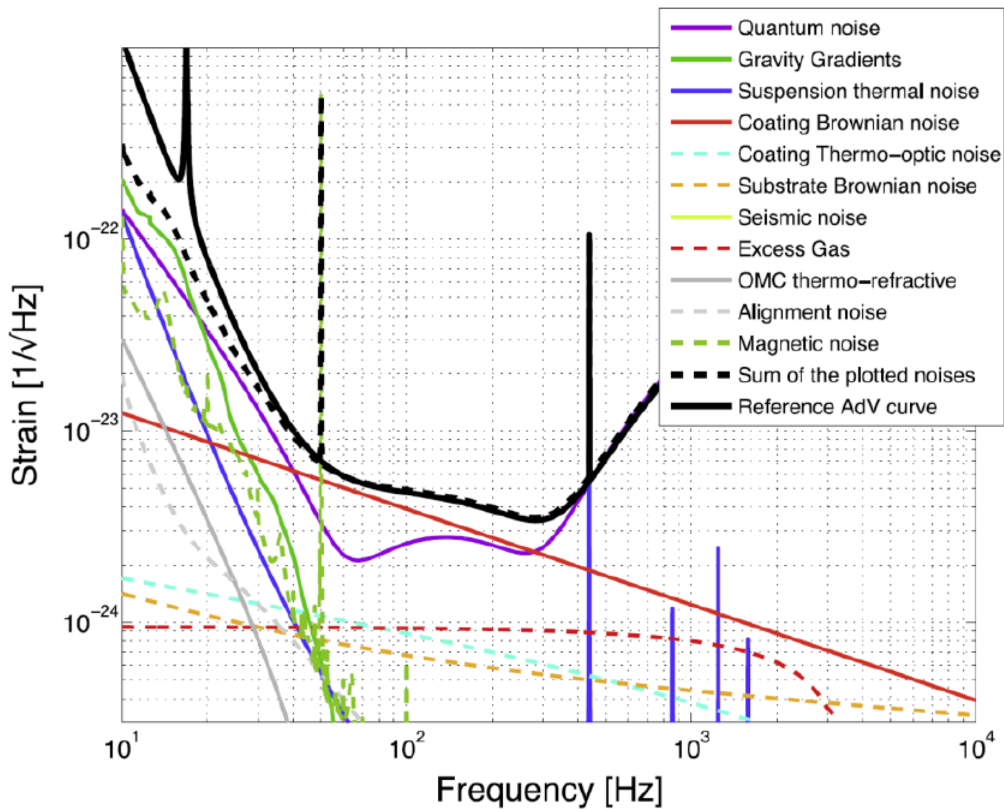

Figure 1.2: Final goal of AdVirgo sensitivity (solid black line), with individual contributions from different kinds of noise. Image from [4].

be incorporated into future detectors to further enhance sensitivity. The various sources of noise in AdVirgo and their impact across different frequencies are illustrated in Fig. 1.2, which also shows the final sensitivity goal. Fig. 1.3 showcases the sensitivity levels of the Virgo and LIGO detectors during the 2020 observing run (O3).

Noise sources can be categorized in several ways, one of which is as follows: fundamental noises that depend on fundamental physical phenomena or are noises that cannot be eliminated without a comprehensive reconfiguration of the interferometer infrastructure. They comprehend seismic, Newtonian, thermal, and quantum noises. And then technical noises are, in principle, manageable and controllable; hence, they typically do not constrain the sensitivity curve if identified and minimized well below the level of fundamental noises. These noises are numerous and result from the quality of the interferometer infrastructure, which also includes stray light.

Primarily dominant at lower frequencies ($< 5\ Hz$) a prevalent source of noise is Newtonian noise. This noise originates from disturbances in the local gravitational field caused by various factors, including movements of air masses in the atmosphere, seismic activity in the soil, human activities, ocean waves, and other perturbations affecting the Earth's gravitational field. Since Newtonian noise displaces the Test Masses directly such a GW, Newtonian noise cannot be shielded. However, it currently does not pose a significant limitation, as other sources of fundamental noises exhibit orders of magnitude higher level across most frequencies in advanced detec-

tors.

At frequencies below $10 - 40\ Hz$, seismic noise emerges as a significant source of noise. This noise results from ground vibrations, stemming from either human activities or natural phenomena, which induce vibrations within the instrument, consequently causing movement in the mirrors and producing phase oscillations in the laser beam. To mitigate this noise, a suspension system for the test masses is employed, comprising a cantilever system with multiple stages of pendulums interconnected to each other, thereby reducing noise at each pendulum level. Thanks to this system, advanced detectors are presently not constrained by seismic noise.

However, in the mid-frequency range $(40 - 300\ Hz)$ thermal noise becomes the dominant factor over seismic noise. This type of noise originates from the material's temperature, leading to slight vibrations correlated with mechanical dissipation in the material, as per the fluctuation-dissipation theorem. This phenomenon principally affects both the mirror's surface and the lowest pendulum of the mirror suspensions. While future detectors might use cryogenic systems to reduce thermal noise, current detectors utilize monolithic suspensions at the end of the pendulum cascade to minimize this effect on the mirror suspension. Despite these efforts, thermal noise remains significant on the mirror surface, prompting ongoing efforts to improve mirror coatings and reduce mechanical losses.

One of the primary sources of noise is quantum noise, which impacts the entire frequency spectrum and becomes dominant at high frequencies (300 Hz - 10 kHz). It arises from the statistical nature of photon counts in the laser beam, following Poissonian statistics, resulting in fluctuations in the phase and amplitude of the light beam. The phase fluctuation, known as shot noise, induces changes in the interference pattern, thereby perturbing the measurement of the GW signal. On the other hand, amplitude fluctuation, termed quantum radiation pressure noise, causes movement of the end mirrors due to varying radiation forces striking the surface. This movement results in phase fluctuations of the reflected beam, further affecting the interference pattern. To mitigate quantum noise, squeezing techniques are employed in both LIGOs and in Virgo during O3, a form of quantum manipulation enabling the reduction of shot noise or radiation pressure noise at the expense of increasing the other. This approach can be adjusted for specific frequencies, allowing for the selection of the most suitable compromise in each frequency band.

Advanced detectors have achieved a sensitivity improvement of approximately an order of magnitude across a wide frequency spectrum. Several enhancements have contributed to this gain in sensitivity, allowing the detection of first gravitational wave signals. One significant feature involves the incorporation of Fabry-Perot cavities in the detector arms. Positioned near the beam splitter at the beginning of each arm, an additional suspended mirror traps photons between the two mirrors, causing them to travel back and forth multiple times before re-entering the beam splitter. This elongates the photon path length, consequently amplifying the absolute change in path length induced by GWs. The integration of Fabry-Perot cavities has notably enhanced detector sensitivity throughout the detection band, particularly at lower frequencies. Fig 1.4 illustrates this enhancement alongside other key optics utilized in the interferometer.

Current second-generation interferometers observe sources mainly consisting of

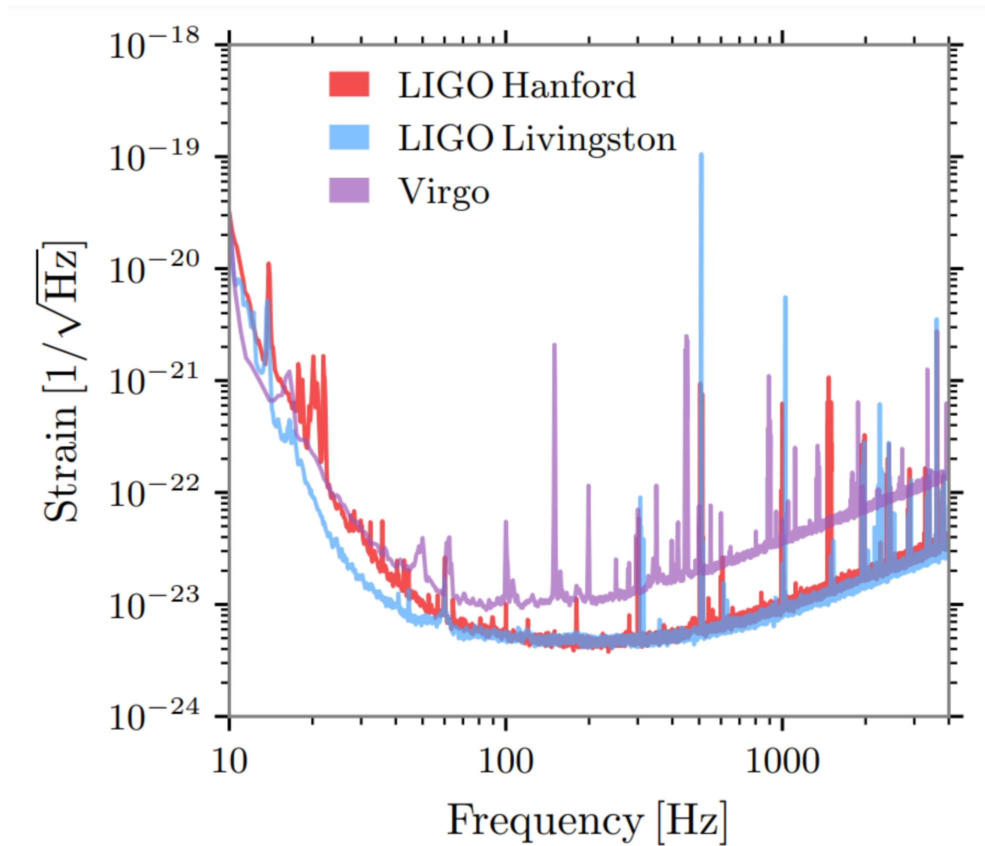

Figure 1.3: Sensitivity of advanced Virgo and LIGO detectors as of 2020. Image from [5]

mergers involving binary systems with black holes and/or neutron stars. Conventionally the sensitivity of gravitational wave detectors is often expressed in terms of the maximum distance at which a binary neutron star (BNS) merger can be observed with a signal-to-noise ratio of 8, known as the BNS range. For the LIGO detectors, this range is currently about 160-170 Mpc, while for the Virgo detector, it is approximately 50 Mpc [6].

Currently, the development of third-generation GW detectors marks a significant leap forward in GW astronomy. These next-generation instruments are designed not only to enhance sensitivity but also to extend the detection bandwidth, with a particular focus on the low-frequency range, including the few Hz range. The expansion of the detection bandwidth aims to capture signals from new types of GW sources and allow the detection of all the GWs generated from compact binaries, with the primary objective on binaries with stellar-mass black holes, allowing crucial investigations into the origins and characteristics of black holes.

An example of a third-generation detector is the Einstein Telescope (ET) [7]. This groundbreaking instrument is being designed with an innovative triangular-shaped interferometer setup, with arms extending up to 10 kilometers. In this way, the instrument will have a disposal of a total of six interferometers, half of which will be designed for high-frequency observations and the remaining half for low-frequency measurements. This triangular design of the detector makes it possible to make autonomously the sky localization, effectively making it an observatory capable

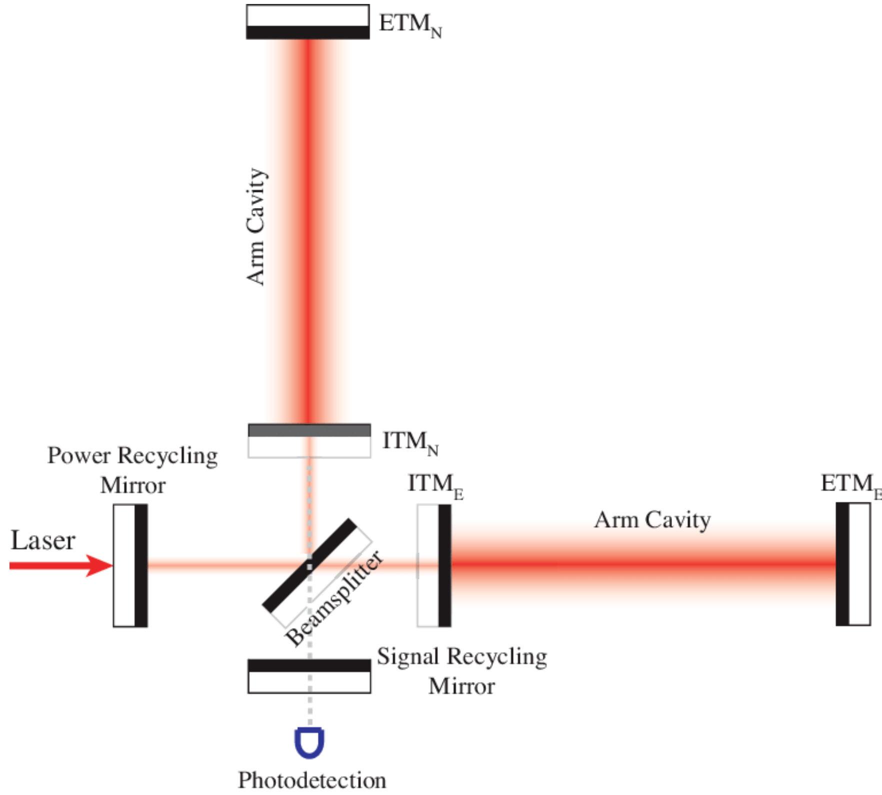

Figure 1.4: Optical scheme of an advanced detector. The most relevant elements are indicated.

of localization the source of gravitational waves, and measuring the polarization of gravitational waves, features currently attainable only by combining data from at least two separate instruments. It will be constructed underground to avoid disturbances from vibrations on the surface. ET's sensitivity is estimated to surpass current second-generation detectors by a factor of 10, potentially detecting tens to hundreds of thousands of GW signals annually, which goes well beyond redshifts at which electromagnetic telescopes can observe individual sources [8].

Detections The output of a GW detector is a time series, where the data are registered in the frequency domain with the associated amplitude, obtained from the characterization of the phase shift of recombined light from the interferometer arms. This output will be a combination of both the desired GW signal and noise, but most of the time the GW signal is way weaker than the noise.

To help significantly improve the signal-to-noise ratio (SNR), data processing is involved. The fundamental technique is matched filtering, which consists of comparing the data with a database of waveform templates, where the templates come from analytical solutions of the strain generated by modeled sources. By discretizing the data and applying filters iteratively, Bayesian analysis [9] is then employed to estimate the parameters of the sources.

For example, in the case of coalescing binaries, the analytical solution of the relation of the GW frequency emitted is [1]:

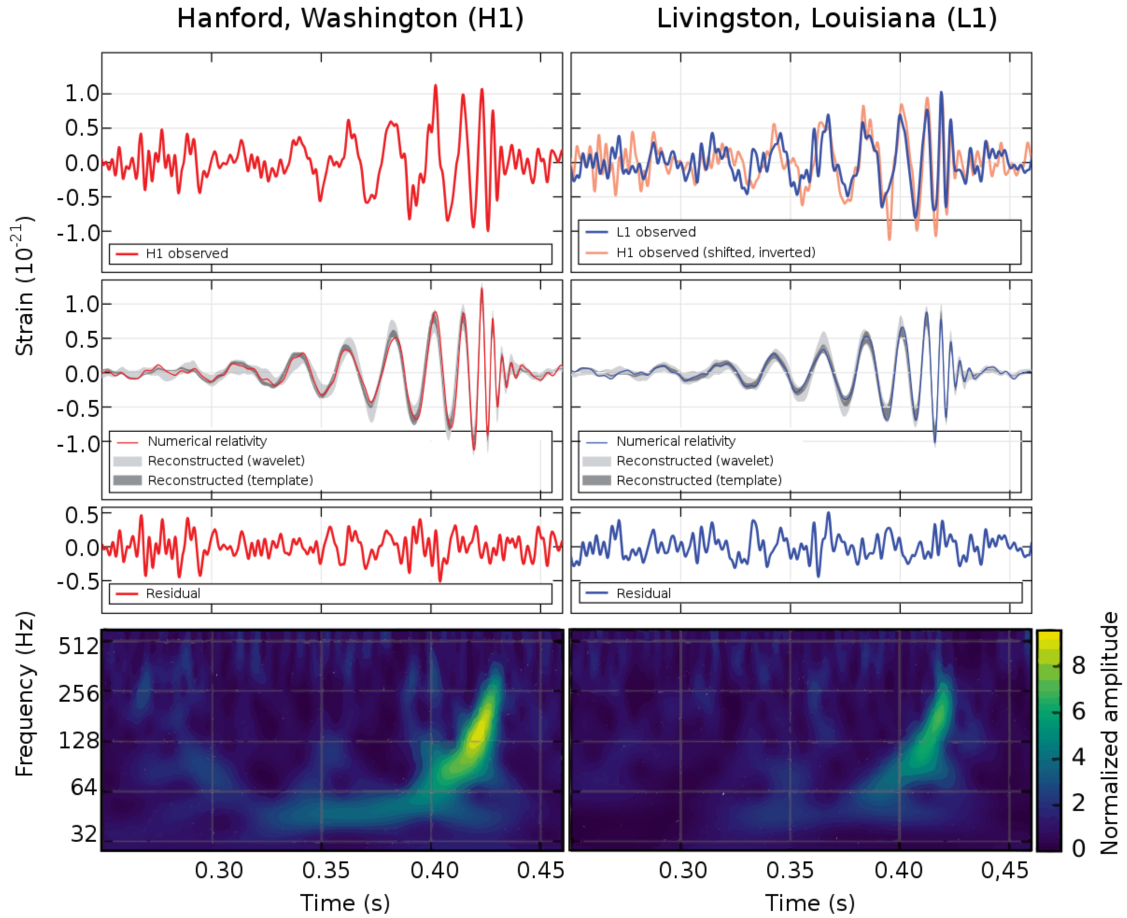

Figure 1.5: Waveform of the GW150914 event observed in the Hanford (H1, left) and Livingston (L1, right) LIGO detectors. The top row displays the observed (filtered) waveform, while the second row presents the numerical relativity reconstruction of the signal, accompanied by the residual from the experimental data. The bottom row shows the Spectrogram of the signal (the power spectral density varying in time). Image from [10]

$$f_{gw}(\tau) = \frac{1}{\pi}\left(\frac{c^3}{GM_c}\right)^{\frac{5}{8}}\left(\frac{5}{256\tau}\right)^{\frac{3}{8}} \tag{1.10}$$

where $\tau = t - t_{coal}$ is the time to coalescence (in particular t_{coal} is the time when the two bodies collide at the end of the inspiral phase) and M_c is the chirp mass of the system, defined as:

$$M_c = \frac{(m_1 m_2)^{3/5}}{(m_1 + m_2)^{1/5}} \tag{1.11}$$

Through this method of data analysis, parameters like mass (m_1, m_2) and distance of the event can be estimated.

Combining the advanced capabilities of interferometer detectors with sophisticated data analysis techniques, in September 2015, a significant milestone in gravitational wave astronomy was achieved with the detection of the first gravitational

wave event, GW150914. The LIGO observatories in Hanford, WA, and Livingston, LA, successfully detected the coincident signal GW150914 (see Fig. 1.5). The event occurred within the intersite propagation time of 10 milliseconds and featured a combined SNR of 24. The peak amplitude of the gravitational wave strain was only $h \cong 10^{-21}$. The waveform characteristics of GW150914 strongly suggest its origin as the result of the merger of two black holes, involving their orbital inspiral, merger, and subsequent formation of a final black hole through ringdown. Over a duration of 0.2 seconds, the signal exhibited a rapid increase in both frequency and amplitude, completing approximately 8 cycles and transitioning from 35 to 150 Hz, reaching its peak amplitude at the latter frequency. The black hole binary components were estimated to have masses of $36M_{\odot}$ and $29M_{\odot}$, respectively. With the limited information from only two detectors, the localization of the source primarily relied on the relative arrival time, resulting in a spatial localization to an area of approximately $600deg^2$ within a 90% credible region [11].

1.3 The issue of straylight

Stray light refers to optical radiation that deviates from its intended path within an optical system, potentially causing unwanted interference during the detection of optical signals. In gravitational wave detectors, stray light issues arise when light from the laser source follows unintended paths relative to the main beam. This stray light is detected as spurious displacement noise, adversely affecting the sensitivity of the detector.

The concern regarding stray light is not exclusive to the latest generation of advanced detectors. It was identified as a critical issue during the design phase of the first-generation gravitational wave detectors back in the 1980s. Over the following 40 years, extensive research has been conducted to better understand and quantify the stray light coupling mechanisms through various analytical and experimental approaches.

Stray light can originate from multiple sources within the optical system. These include secondary beams or spurious reflections caused by imperfect anti-reflective coatings on optics, diffuse reflections from rough mirror surfaces, scattering due to micro-defects such as dust, scratches, or ditches, and diffraction at the edges of optics, which inherently have limited apertures. Moreover, complex configurations may emerge when light undergoes multiple scatterings before re-entering the main beam path. The generation of stray light can be categorized by two primary processes: specular reflection and incoherent scattering. Examples of stray light sources are depicted in Fig. 1.6.

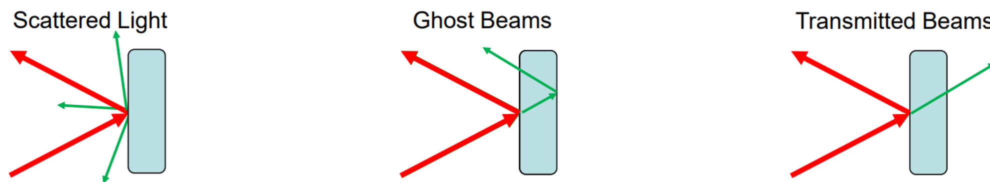

Figure 1.6: Examples of stray light generation mechanism.

To mitigate the impact of stray light noise, several strategies can be employed, often in combination. These include optimizing the design of low-scattering optics, implementing beam dumps and baffles, reducing the motion of stray light sources through enhanced suspension and motion control systems, improving anti-reflective coatings, and enhancing optical isolation with devices such as Faraday Isolators.

Advanced optical simulations that incorporate realistic surface maps and employ techniques such as FFT propagation of the laser field are crucial for understanding stray light generation mechanisms. Additionally, statistical methods can be used to predict the angular distribution of scattered light, providing further insights into the management and reduction of stray light within gravitational wave detectors.

Straylight recombination mechanism Understanding the mechanisms through which stray light can influence interferometric signals is crucial. At first glance, the recoupling of stray light with the main beam may not appear problematic. However, issues arise when the stray light originates from a component that possesses its own motion. In these cases, the stray light carries phase information that is influenced by the length of the scattering path, which is further modulated by the motion of the scattering element $z_s(t)$ [12]:

$$\phi_s(t) = \phi_0 + \frac{4\pi}{\lambda} z_s(t) \tag{1.12}$$

In the interferometer, the stray light field E_s adds with the unperturbed field E_{in} at a reference point p:

$$E_p = E_{in} + E_s e^{i\phi_s(t)} = E_{in}\left[1 + \frac{E_s}{E_{in}} e^{i\phi_s(t)}\right] = E_{in}\left[1 + \sqrt{\frac{P_s}{P_{in}}} e^{i\phi_s(t)}\right] \tag{1.13}$$

In the final equality, the phase difference between the two fields is factored out and incorporated into the static contribution to the scattering phase, ϕ_0, as described in Eq. 1.12.

As a condition generally expected in interferometric detectors, it can be safely assumed that the amount of scattering is small:

$$\sqrt{\frac{P_s}{P_{in}}} \ll 1 \tag{1.14}$$

This allows us to recognize that the leftmost term in Eq. 1.13 is the first-order expansion of an exponential:

$$E_p = E_{in} \exp\left[\sqrt{\frac{P_s}{P_{in}}} (cos\phi_s(t) + i\, sin\phi_s(t))\right] \tag{1.15}$$

The effect of recoupled stray light is embedded within the exponential term, leading to additional modulation of the laser field. Since the exponent contains both real and imaginary parts, both the phase and amplitude of the field undergo modulation. If the motion of the scattering element is small, the sine and cosine functions can be approximated by their arguments, allowing for a linear dependence

of the added noises on the motion. This linear approximation is easier to handle. However, as the amplitude of the motion increases, this first-order approximation becomes inadequate. The effects of quadratic and higher-order couplings begin to emerge, which are more complex and challenging to model accurately.

The aim of this thesis is to investigate the mechanisms underlying the generation of stray light. Firstly, the focus will be on examining theoretical models of scattering phenomena from surfaces and various types of material, followed by experimental investigation of the behavior of the scattering properties of surface samples. In this context, I worked on the development and improvement of a scatterometer, an instrument designed to measure the angular distribution of the intensity of scattered light from examined samples. In particular, I helped optimize the instrument's background measurement, enhancing its sensitivity. I started characterizing the scattering properties of surfaces, including samples representative of the components used in the Virgo detector. Future prospects of this research program involve improving the investigation of stray light by stray light simulation analyses to the experimental measurements.

Chapter 2

Straylight

Scattered light phenomena occur when light encounters the boundary between two distinct media or light traverses regions made of inhomogeneous materials. Upon this interaction, a portion of incident light is reflected into the originating medium, while another fraction continues its trajectory through the medium.

Under ideal conditions of a smooth surface boundary, the reflection and refraction of light follow the precise rules defined by Fresnel's equations and Snell's law, respectively. However, if the surface is irregular, part of the light deviates from the expected path predicted by these laws, resulting in what is called surface scattering. This departure from predicted behavior also happens in mediums that are inhomogeneous or a mixture of materials of different dielectric properties, where a portion of the light undergoes reflection and refraction within the inhomogeneous medium. This is referred to as volume scattering. Usually, both kinds of scattering are present.

An example of a heterogeneous medium is a volume filled with air, where volume scattering is caused by the individual gas molecules. As we scale up, dust particles in the air also induce scattering. In addition, these particles can deposit on surfaces, increasing the scattering which may be already present because of surface roughness. Moreover, the deposition of particles onto surfaces and the existence of imperfections such as scratches amplify scattering effects, thus adding complexity to the optical behavior of the system.

Notably, these scattering phenomena exhibit different dependencies on wavelength, necessitating a comprehensive understanding of scattering mechanisms across the electromagnetic spectrum.

2.1 Basic Radiometry

The final goal of this work is to quantify the amount of scattered light produced by materials and dust contamination. This is achieved through the usage of two important quantities: the Bidirectional Scattering Distribution Function (BSDF) and the total integrated scattering (TIS). Before delving into the examination of the quantities that describe the scattered light, it is necessary to introduce fundamental radiometric quantities and concepts.

- **Flux**

  Flux or power quantifies the rate of energy transfer per unit of time. It is commonly expressed in units of Joules per second (Js^{-1}) or Watts (W). Its formal definition is:

$$d\phi = \frac{dQ(t)}{dt} \tag{2.1}$$

  where Q(t) is the energy of the electromagnetic field and t is the time.

- **Radiance**

  Radiance refers to the flux emitted by a surface in a specific direction. When observing an object at an angle θ from the normal of the emitting surface, the surface area visible to the observer is the projected area $A\, cos\theta$, where A represents the true surface area of the emitter. The receiver's surface area defines a solid angle Ω as seen from the emitting surface (see also Fig. 2.1); the radiance of the latter is defined as the flux per unit projected area and unit solid angle. Mathematically, its formal definition is:

$$L = \frac{d^2\phi}{dA\, cos\theta\, d\Omega} \tag{2.2}$$

  Radiance is commonly measured in units of Watts per steradian per square meter ($Wsr^{-1}m^{-2}$). An emitter that has constant radiance at all directions θ is referred to as a Lambertian emitter.

- **Irradiance**

  Irradiance represents the flux per unit area received by a surface. Unlike radiance, it does not depend on direction. Mathematically, it can be expressed as:

$$E = \frac{d\phi}{dA} \tag{2.3}$$

  It is commonly quantified in units of Watts per square meter (Wm^{-2}).

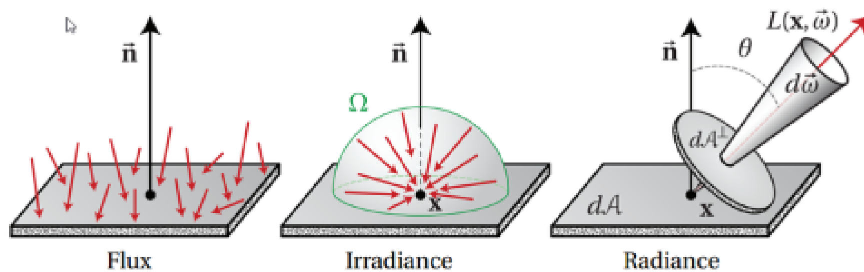

Figure 2.1: 3D visualization the definition of flux, radiance and irradiance. Image source [13]

BSDF and TIS Two important quantities that are used to characterize the scattering are: the bidirectional scattering distribution function (BSDF) and the total integrated scattering (TIS).

The BSDF was introduced by Nicodemus in 1970 and is expressed as:

$$BSDF(\theta_i, \phi_i, \theta_s, \phi_s) = \frac{dL(\theta_i, \phi_i, \theta_s, \phi_s)}{dE(\theta_i, \phi_i)} \tag{2.4}$$

Here, dL represents the differential radiance of the surface, while dE denotes the differential irradiance incident on the surface. These quantities are dependent on the angles θ_i and ϕ_i, which represent the elevation and azimuth angles of the incident light, and θ_s and ϕ_s, which correspond to the scattered beam (Fig. 2.2).

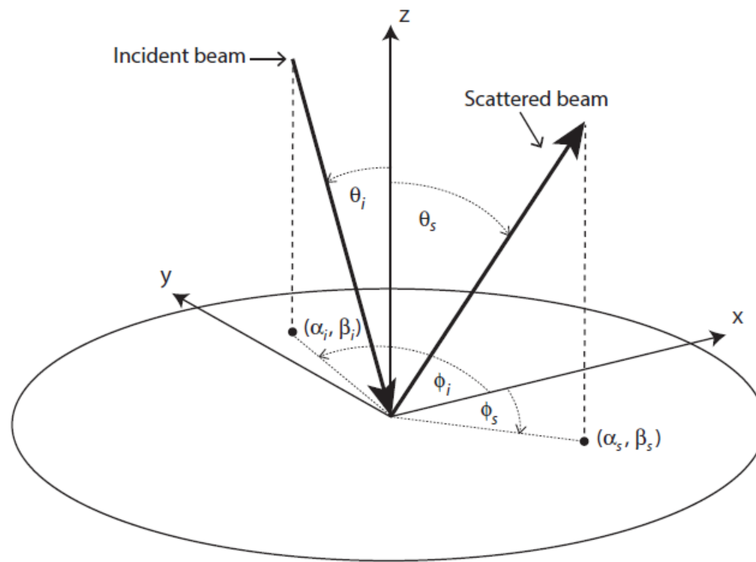

Figure 2.2: Angles used in the definition of the BSDF. Image from [14]

Essentially The BSDF describes how light scatters in all directions when it interacts with a surface. It is a function that characterizes the distribution of scattered light as a function of both incident and outgoing directions. In other words, the BSDF provides information about how light is scattered from a surface in response to incident light from various directions.

When discussing surface scattering, the BSDF can be segmented into two components (Fig. 2.3): the bidirectional reflectance distribution function (BRDF), which accounts for the reflected portion of radiation, and the bidirectional transmittance distribution function (BTDF), which considers the radiation transmitted through the material's surface. These definitions can be similarly applied to volume scattering, with distinctions made based on the direction of scattering relative to the incident light.

The BSDF provides a comprehensive description of a surface's scattering properties, making it a valuable tool for characterizing the scattering behavior of a system. This is particularly crucial as the performance of an optical system regarding stray light is often heavily influenced by the BSDF of its components.

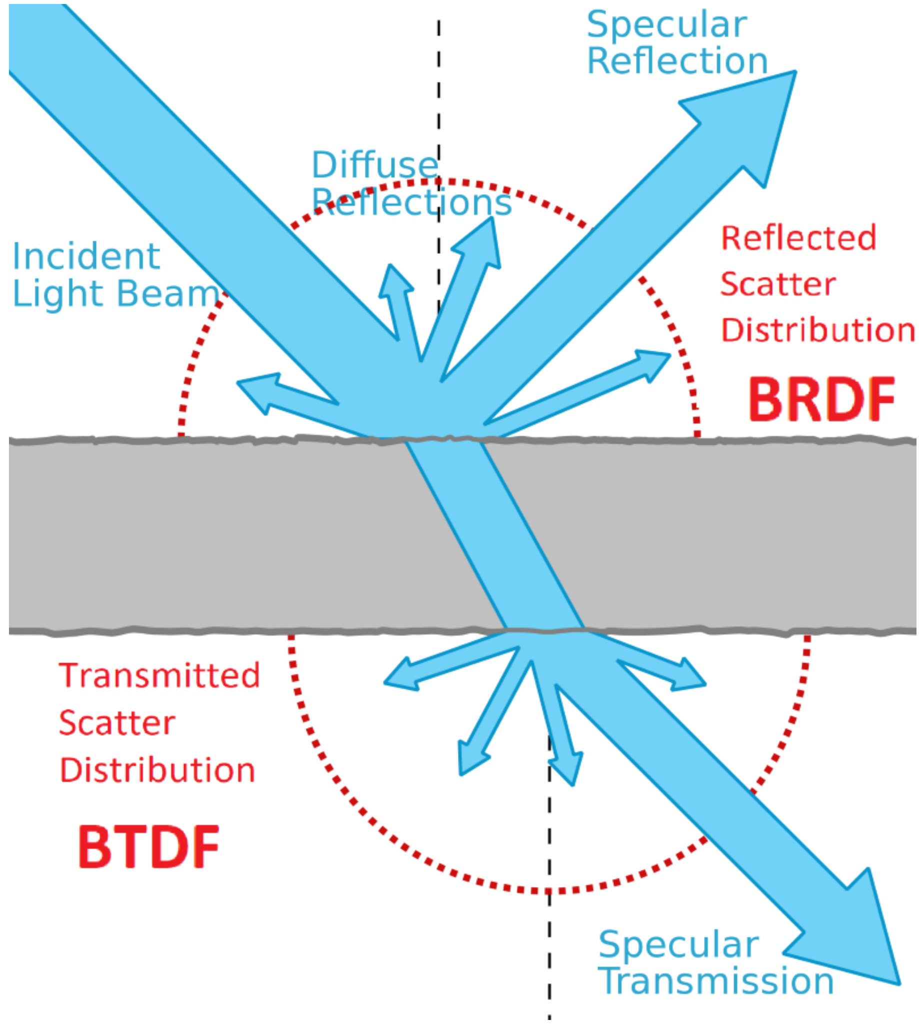

Figure 2.3: Pictorial representation of the BRDF and BTDF contributions separately; the BSDF is the sum of the two (image from [15]).

On the other hand, TIS refers to the overall scattering of light from a surface over all possible angles within one hemisphere of the sphere, covering either the reflected or the transmitted scatter. TIS integrates the scattering contributions from all angles within this hemisphere and provides a comprehensive measure of the surface's scattering behavior within that particular region. It can be expressed as the integral of the BSDF over the relevant hemisphere:

$$TIS(\theta_i, \phi_i) = \int_0^{2\pi} \int_0^{\pi/2} BSDF(\theta_i, \phi_i, \theta_s, \phi_s) \cos(\theta_s) \sin(\theta_s) \, d\theta_s d\phi_s \tag{2.5}$$

The Total Integrated Scattering (TIS) indicates the portion of the total incident power that is scattered by the surface within a specific hemisphere. It can alternatively be expressed as:

$$TIS = \frac{P_{scatt}}{P_{tot}} \tag{2.6}$$

Since TIS is the ratio of two powers, it is a dimensionless quantity, bounded between 0 and 1, ensuring conservation of energy.

2.2 Scattering from Roughness

The curvature or deviation of an optical surface is typically expressed as the combination of two profiles: its optical figure profile and its surface roughness profile, illustrated in Fig. 2.4. The optical figure profile defines the surface's image-forming characteristics and determines the direction of specularly reflected or transmitted rays. It represents the regular and deterministic shape of the surface, and it can be described using a general conic equation, along with any additional aspheric terms. The surface roughness profile, on the other hand, governs the intensity and angular spread of light scattered from the surface. It represents the deviations from the optical figure with smaller spatial frequencies and can be described by stochastic models. We denote the deviation due to the surface roughness as $z(x, y)$, at different points (x, y) on the surface.

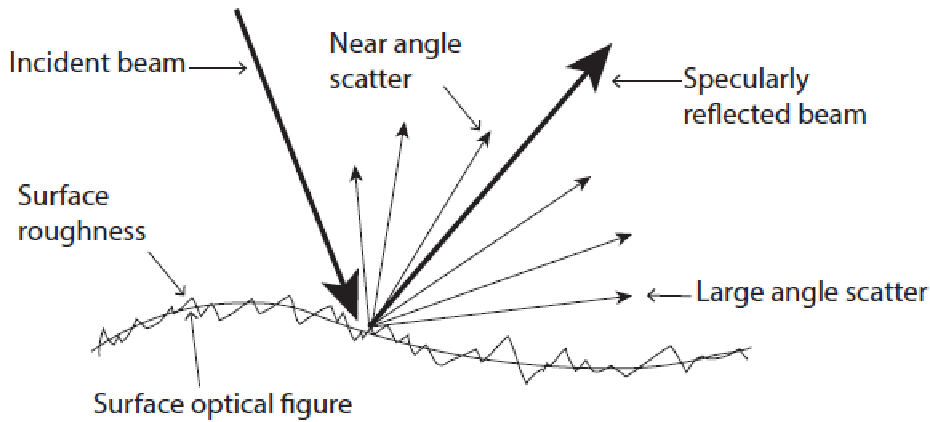

Figure 2.4: Scattering from surface roughness. Image from [14]

2.2.1 Roughness model

Two significant quantities that can be computed from the function profile $z(x, y)$ are its power spectral density (PSD) and the root mean square (RMS) roughness of the surface. The PSD, denoted as S_2, characterizes the distribution of spatial frequencies within the profile $z(x, y)$. It is defined as the modulus squared of the Fourier transform of the surface roughness:

$$S_2(f_x, f_y) = \lim_{L \to \infty} \frac{1}{L^2} \left| \int_{-L/2}^{L/2} \int_{-L/2}^{L/2} z(x, y) \, \exp[-2\pi i (f_x x + f_y y)] \, dx \, dy \right|^2 \tag{2.7}$$

with spatial frequencies f_x and f_y and a length L representing the spatial extension of the measured profile.

The RMS roughness quantifies the average deviation of the surface from its ideal height. It is computed as the square root of the integral of the profile z(x,y) over its area, normalized by the area itself:

$$\sigma = \left\{ \lim_{L\to\infty} \frac{1}{L^2} \int_{-L/2}^{L/2} \int_{-L/2}^{L/2} [z(x,y)]^2 \, dx \, dy \right\}^{1/2} \tag{2.8}$$

It can be proven that the RMS is also equal to the square root of the integral of the PSD over all spatial frequencies:

$$\sigma = \left\{ \int_{-\infty}^{\infty} \int_{-\infty}^{\infty} S_2(f_x, f_y) \, df_x \, df_y \right\}^{1/2} \tag{2.9}$$

The roughness function of a surface is influenced by the finishing process it undergoes and is typically more challenging to predict compared to the surface figure. Polished surfaces created using standard methods on glassy materials typically display an inverse power law trend in their PSD. This behavior can be effectively described using the well-known "ABC function" or "K-Correlation function". This model's functional form is defined as

$$S_2(f) = A[1 + (Bf)^2]^{-C/2} \tag{2.10}$$

where $f = (f_x^2 + f_y^2)^{1/2}$.

A represents the magnitude of the PSD at low frequencies (as illustrated in Fig. 2.5), $1/B$ denotes the spatial frequency at which the "roll-off" of the function occurs, and C represents the slope of the PSD at frequencies above $1/B$.

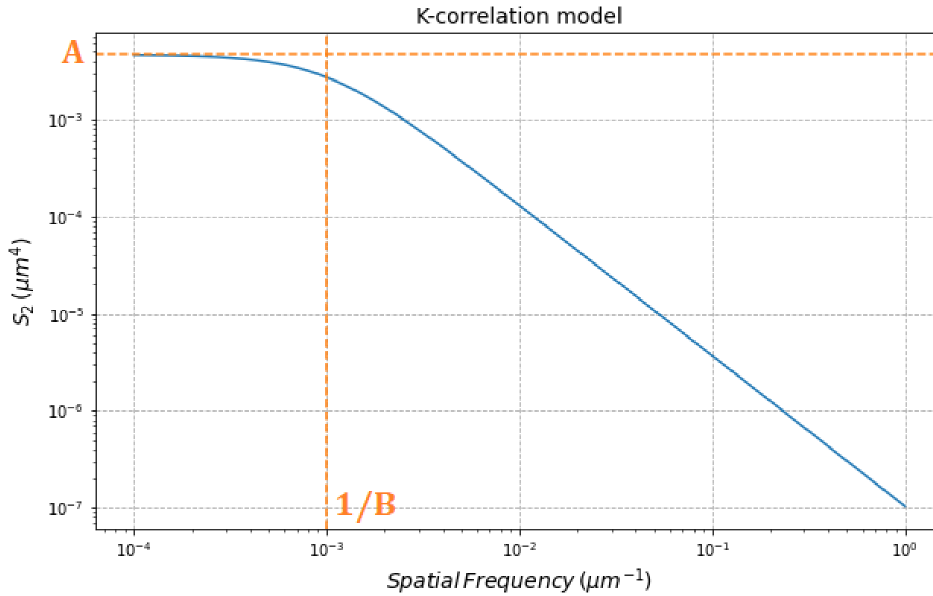

Figure 2.5: Simulated PSD S_2 versus spatial frequency f for a typical mirror surface with $\sigma = 13.1\mathring{A}$. The k-correlation model parameters are $A = 4.64 \times 10^{-3} \mu m^4$, $1/B = 10^{-3} \mu m^{-1}$, and $C = 1.55$.

2.2.2 Scattering model - Harvey-Shack

The "Harvey-Shack model" is frequently discussed in the literature as a parametrization of the Rayleigh-Rice perturbation theory [14]. In this model, the BRDF is directly proportional to the PSD of the surface roughness.

To illustrate this relationship, we begin by considering a planar surface, with the (x, y) plane corresponding to the surface plane of the sample. We employ spherical coordinates where the polar angle is $\theta \in [0, \pi]$ and the azimuthal angle is $\phi \in [0, 2\pi]$. The relationship between the PSD and the BSDF, in the regime where the roughness scale is much smaller than the wavelength of light $\sigma \ll \lambda$, is expressed as:

$$BSDF(\theta_i; \theta_s, \phi_s) = \frac{16\pi^2 \Delta n^2}{\lambda^4} \cos\theta_i \cos\theta_s \, Q \, S_2(f_x, f_y) \tag{2.11}$$

In this context, Q represents the polarization-dependent reflectance of the surface, Δn stands for the difference in refractive index between the scatterer's material and the surrounding medium, λ denotes the wavelength, and S_2 signifies the 2-dimensional PSD of the surface. Here, ϕ_i is assumed to be zero for simplicity. Under the assumption of surface isotropy, modifying the value of ϕ_i only results in the rotation of the BRDF around the z-axis, without altering its overall shape.

In the case of 2D geometry we can parametrize:

$$f_x = \frac{sin\theta_s cos\phi_s - sin\theta_i}{\lambda} \tag{2.12}$$

and

$$f_y = \frac{sin\theta_s sin\phi_s}{\lambda} \tag{2.13}$$

Note the similarity between these equations and the general grating equation, expressed as:

$$f = \frac{|sin\theta_s - sin\theta_i|}{m\lambda} \tag{2.14}$$

Here, m signifies the order of the diffracted beam. Consequently, the Rayleigh-Rice perturbation theory treats the optical surface as a collection of diffraction gratings of different frequencies. Surfaces that exhibit scattering behavior dependent on $|sin\theta_s - sin\theta_i|$ are termed as shift invariant.

In most cases, the BSDF calculated by Eq. 2.11 aligns closely with experimental observations. Given that the scattering from the majority of optical surfaces tends to be isotropic and their roughness is typically well characterized by the K-correlation model, Eq. 2.11 can be expressed as:

$$\begin{aligned} BSDF(\theta_s, \theta_i) = & \frac{16\pi^2 \Delta n^2}{\lambda^4} \cos\theta_s \cos\theta_i Q \\ & \times \left\{ A \left[1 + \left(\frac{B|\sin\theta_s - \sin\theta_i|}{\lambda} \right)^2 \right]^{-C/2} \right\} \end{aligned} \tag{2.15}$$

The term $cos(\theta_i)cos(\theta_s)$ is known as the "obliquity factor". As a result, the functional form of BSDF versus $|\sin\theta_s - \sin\theta_i|$ is similar to the function form of PSD versus f (Fig. 2.6).

Eq. 2.15 is commonly parametrized as the 3-parameter Harvey model, also called the Harvey-Shack model:

$$BSDF(\theta_s,\theta_i) = cos(\theta_i)cos(\theta_s)b_0\left[1+\left(\frac{|\sin\theta_s - \sin\theta_i|}{l}\right)^2\right]^{s/2} \tag{2.16}$$

where the definitions of the parameters are:

$$b_0 = \frac{16\pi^2\Delta n^2 QA}{\lambda^4}, \tag{2.17}$$

$$l = \frac{\lambda}{B}, \tag{2.18}$$

$$s = -C. \tag{2.19}$$

A straightforward solution for the TIS of a Harvey scatterer at $\theta_i = 0$ can be obtained by substituting Eq. 2.16 into Eq. 2.5. For $s = -2$

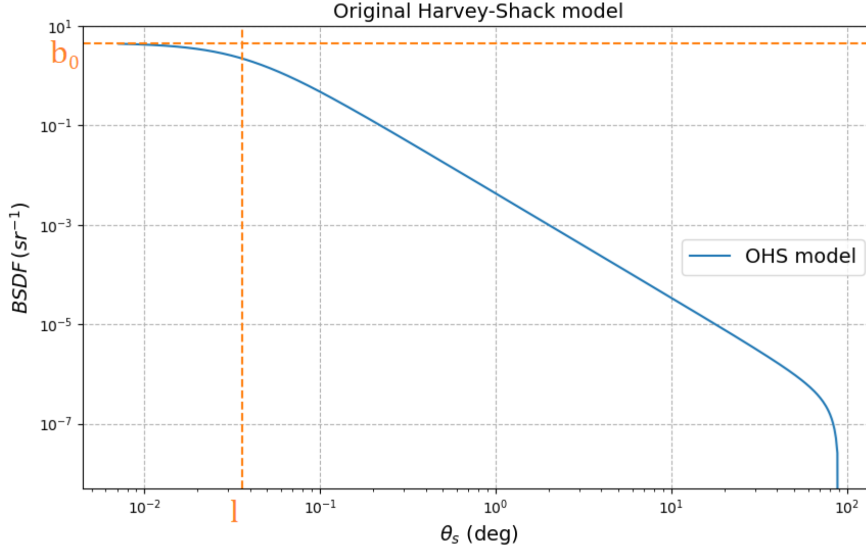

Figure 2.6: Simulated BRDF versus $|sin\theta_s - sin\theta_s|$ for the 13.1Å-RMS roughness mirror whose PSD is given in Fig. 2.5 ($\lambda = 0.6328\mu m$, $\Delta n = 2$, and $sin(\theta_i) = 1$).

$$TIS = \frac{2\pi b_0}{l^s(s+2)}\left[(1+l^2)^{\frac{s+2}{2}} - (l^2)^{\frac{s+2}{2}}\right] \tag{2.20}$$

and $s = 2$

$$TIS = \pi b_0 l^2 ln\left(1+\frac{1}{l^2}\right) \tag{2.21}$$

At $\theta_i \neq 0$, numerical evaluation is necessary to determine the TIS.

2.2.3 Generalized Harvey-Shack Model

The parameterization of the Rayleigh-Rice perturbation theory using the Harvey-Shack model, as derived in the previous section, is commonly referred to as the Original Harvey-Shack (OHS) model. The OHS model was developed by James E. Harvey and Roland V. Shack in 1976 as a linear systems diffraction BRDF model [18]. This model implicitly assumes low scattering angles, which poses a limitation for the purposes of this work. To address the limitations of the OHS model, particularly its assumption of low scattering angles, the Generalized Harvey-Shack (GHS) model was developed by Krywonos in 2011. The GHS model accommodates larger scattering and incidence angles, as well as both smooth and rough surfaces, and different forms of the PSD. It describes scattering through a surface transfer function that relates the scattered field to the input field, based on the properties of the surface. This subsection provides an overview of this model, but the detailed derivation of the GHS model can be found in [16].

The GHS surface scatter theory employs a two-parameter family of surface transfer functions to characterize the scattering behavior of light from surfaces that are arbitrarily rough and for incident and scattered angles that are arbitrarily large:

$$H(\hat{x}, \hat{y}; \gamma_i, \gamma_s) = \exp\left\{ - \left[2\pi\sigma_{\mathrm{rel}}(\gamma_i + \gamma_s)\right]^2 \left[1 - \frac{C_s(\hat{x}, \hat{y})}{\sigma_s^2}\right] \right\}, \tag{2.22}$$

Here $\gamma_i = cos\theta_i$, $\gamma_s = cos\theta_s$, σ_{rel} is the band-limited relevant RMS surface roughness (divided by the wavelength), $C_s(x, y)$ is the surface autocovariance (ACV) function and σ_s is the total intrinsic RMS surface roughness. Note that a scaled coordinate system has been used in which the spatial variables are normalized by the wavelength of the light ($\hat{x} = x/\lambda$, $\hat{y} = y/\lambda$, etc.). The reciprocal variables α and β are thus the direction cosines of the propagation vectors of the angular spectrum of plane waves. These directions cosines α, β, and γ are related to the angular variables θ and ϕ in conventional spherical coordinates by the following expressions:

$$\alpha = \sin\theta\,\cos\phi, \quad \beta = \sin\theta\,\sin\phi, \quad \gamma = \cos\theta. \tag{2.23}$$

The relevant roughness is the portion of the RMS roughness that contributes to the BRDF. Scattering beyond 90° from the surface normal does not contribute to the reflected diffused light, so the waves that do contribute meet the condition $\alpha_s^2 + \beta^2 < 1$. By combining this with the grating equation, it is evident that the spatial frequencies contributing to the BRDF lie within a circular boundary of radius $1/\lambda$ in spatial frequency space, centered at:

$$\hat{f}_0 = \frac{\sin\theta_0}{\lambda}. \tag{2.24}$$

With $\theta_0 = -\theta_i$. The relevant roughness is defined as the square root of the integral of the surface PSD over the relevant frequency section:

$$\sigma_{\mathrm{rel}}(\lambda, \theta_i) = \sqrt{\int_{-1/\lambda+f_0}^{1/\lambda+f_0} \int_{-\sqrt{1/\lambda^2-(f_x-f_0)^2}}^{\sqrt{1/\lambda^2-(f_x-f_0)^2}} S_2(f_x, f_y) df_x df_y}. \tag{2.25}$$

Focusing on the reflected part of BSDF, the BRDF is given by the surface reflectance, R, times the angle spread function ASF:

$$\mathrm{BRDF}(\alpha_s, \beta_s; \gamma_i, \gamma_s) = R\,\mathrm{ASF}(\alpha_s, \beta_s; \gamma_i, \gamma_s), \tag{2.26}$$

The ASF is given by invoking the shift theorem of Fourier transformation of the transfer function $H(\hat{x}, \hat{y}; \gamma_i, \gamma_s)$:

$$\mathrm{ASF}(\alpha_s, \beta_s; \gamma_i, \gamma_s) = \mathcal{F}\{H(\hat{x}, \hat{y}; \gamma_i, \gamma_s)\exp(-i2\pi\beta_0\hat{y})\}\Big|_{\alpha=\alpha_s, \beta=\beta_s}. \tag{2.27}$$

The surface transfer function can be written in the form of a Strehl factor, $A(\gamma_i, \gamma_s)$, representing the energy contained in the specular reflection, plus a constant $B(\gamma_i, \gamma_s)$ (the total integrated scatter) times a scattered term, $G(\hat{x}, \hat{y}; \gamma_i, \gamma_s)$, that describes the shape of the scattering function:

$$H(\hat{x}, \hat{y}; \gamma_i, \gamma_s) = A(\gamma_i, \gamma_s) + B(\gamma_i, \gamma_s)G(\hat{x}, \hat{y}; \gamma_i, \gamma_s) \tag{2.28}$$

with:

$$A(\gamma_i, \gamma_s) = \exp\left\{-[2\pi(\gamma_i + \gamma_s)\sigma_{\mathrm{rel}}]^2\right\}, \tag{2.29}$$

$$B(\gamma_i, \gamma_s) = 1 - A(\gamma_i, \gamma_s), \tag{2.30}$$

$$G(\hat{x}, \hat{y}, \gamma_i, \gamma_s) = \frac{e^{-[2\pi(\gamma_i+\gamma_s)\sigma_{\mathrm{rel}}/\sigma_s]^2 C_s(\hat{x},\hat{y})} - 1}{e^{-[2\pi(\gamma_i+\gamma_s)\sigma_{\mathrm{rel}}]^2} - 1}. \tag{2.31}$$

Using the above definitions, the ASF can thus be written as:

$$\mathrm{ASF}(\alpha_s, \beta_s; \gamma_i, \gamma_s) = A(\gamma_i, \gamma_s)\delta(\alpha_s, \beta_s - \beta_0) + K(\gamma_i)S(\alpha_s, \beta_s; \gamma_i, \gamma_s), \tag{2.32}$$

where the Dirac-delta function describes the specularly reflected peak. $S(\alpha_s, \beta_s; \gamma_i, \gamma_s)$ is the scattering function and is given by:

$$S(\alpha_s, \beta_s; \gamma_i, \gamma_s) = B(\gamma_i, \gamma_s)\mathcal{F}\{G(\hat{x}, \hat{y}, \gamma_i, \gamma_s)e^{-i2\pi\beta_0\hat{y}}\}. \tag{2.33}$$

$K(\gamma_i)$ is a renormalization constant that is required by Parseval's theorem to ensure the integral of $S(\alpha_s, \beta_s; \gamma_i, \gamma_s)$ equals the real and measurable value of the TIS. It is given by:

$$K(\gamma_i) = B(\gamma_i, \gamma_s)\left(\int_{-1}^{1}\int_{-\sqrt{1-\alpha_s^2}}^{\sqrt{1-\alpha_s^2}} S(\alpha_s, \beta_s; \gamma_i, \gamma_s)\,d\alpha_s d\beta_s\right)^{-1}. \tag{2.34}$$

Since the BRDF, defined as the scattered radiance divided by the incident irradiance, is determined by the reflectance multiplied by the Fourier transform of the surface transfer function, predicting the scattered light behavior can be computationally intensive. However, if the surface roughness is isotropic, the surface transfer function becomes rotationally symmetric, simplifying the two-dimensional Fourier transform to a one-dimensional Hankel transform [17].

Smooth-surface Approximation When the roughness of the surface is small compared to the wavelength of the incident light ($\sigma_{rel} \ll \lambda$), the surface transfer function is still described by Eq. 2.28. However, explicit approximations can be made to its components expressed in Eq. 2.29, Eq. 2.30, and Eq. 2.31:

$$A(\gamma_i, \gamma_s) \approx 1 - [2\pi\sigma_{\text{rel}}(\gamma_i + \gamma_s)]^2, \tag{2.35}$$

$$B(\gamma_i, \gamma_s) \approx [2\pi\sigma_{\text{rel}}(\gamma_i + \gamma_s)]^2, \tag{2.36}$$

$$G(\hat{x}, \hat{y}) \approx \frac{C_s(\hat{x}, \hat{y})}{\sigma_s^2}. \tag{2.37}$$

Excluding the specular reflection, as this is the standard definition of BRDF, therefore, the first term in Eq. 2.32 is omitted, the ASF results in:

$$\text{ASF}(\alpha_s, \beta_s; \gamma_i, \gamma_s) = K(\gamma_i) S(\alpha_s, \beta_s; \gamma_i, \gamma_s). \tag{2.38}$$

With the approximations and writing the Fourier transform operation in integral form, can be factored out the σ_s^2 and also a $1/\lambda^2$ from the $d\hat{x}d\hat{y}$ inside the Fourier transform operation to obtain the expression for $S(\alpha_s, \beta_s; \gamma_i, \gamma_s)$:

$$S(\alpha_s, \beta_s; \gamma_i, \gamma_s) = [2\pi\sigma_{\text{rel}}(\gamma_i + \gamma_s)]^2 \frac{K(\gamma_i)}{\lambda^4 \sigma_s^2} \mathcal{F}\{C_s(\hat{x}, \hat{y}) e^{-i2\pi\beta_0 \hat{y}}\}, \tag{2.39}$$

where

$$\mathcal{F}\{C_s(\hat{x}, \hat{y}) e^{-i2\pi\beta_0 \hat{y}}\}(\alpha_s, \beta_s) = \frac{1}{2\pi} \int_{-\infty}^{\infty} \int_{-\infty}^{\infty} C_s(\hat{x}, \hat{y}) e^{-i2\pi(\alpha_s \hat{x} + (\beta_s + \beta_0)\hat{y})} d\hat{x} d\hat{y}. \tag{2.40}$$

This integral represents a Fourier transform, with the frequency variable in the y-direction translated from β_s to $\beta_s + \beta_0$. This translation results in a shift in the scattered radiance within the direction cosine space. Since the form of the BRDF remains unchanged, this is equivalent to the Fourier transform of the ACV function, which corresponds to the PSD.

Therefore,

$$\text{ASF}(\gamma_s, \gamma_i; \hat{f}_x, \hat{f}_y) = [2\pi\sigma_{\text{rel}}(\gamma_i + \gamma_s)]^2 \frac{K(\gamma_i)}{\lambda^4 \sigma_s^2} S_2(\hat{f}_x, \hat{f}_y), \tag{2.41}$$

and the scattering function becomes proportional to the surface PSD function, similar to the RR model. Substituting this expression for the ASF in Eq. 2.26, and writing the PSD using the K correlation model, we have:

$$\text{BRDF}(\gamma_i, \gamma_s; f) = RK(\gamma_i) \frac{[2\pi\sigma_{\text{rel}}(\gamma_i + \gamma_s)]^2}{\lambda^4 \sigma_s^2} A \left[1 + \left(\frac{B}{\sqrt{f_x^2 + f_y^2}}\right)^2\right]^{C/2}. \tag{2.42}$$

For a certain angle of incidence, this can be parameterized as:

$$b_0 = RK(\gamma_i) \frac{[4\pi\sigma_{\text{rel}}]^2}{\lambda^4 \sigma_s^2} A, \tag{2.43}$$

$$l = \frac{\lambda}{B}, \tag{2.44}$$

$$s = -C. \tag{2.45}$$

The final expression for the GHS model of the BRDF with the smooth-surface approximation is then:

$$\mathrm{BRDF}(\theta_s, \phi_s, \theta_i) = b_0 \frac{(\cos\theta_i + \cos\theta_s)^2}{4} \left(1 + \left[\frac{|\sin\theta_s - \sin\theta_i|}{l}\right]^2\right)^{s/2}, \tag{2.46}$$

where the same assumptions of the OHS model, $\phi_i = 0$ and surface isotropy, are used. The obliquity factor in this context is $(\cos\theta_i + \cos\theta_s)^2$. It has been shown that the obliquity factor in the RR model in Eq. 2.11 is an approximation of this. The RR theory assumes that the wavelength of the scattered light is shorter than the surface autocovariance length, leading to this approximation in the obliquity term. Consequently, the BRDF assumes the same form as the expression derived from the RR theory. In Fig. 2.7 it is shown the comparison between the OHS model described by Eq. 2.11 and the GHS model described by Eq. 2.46.

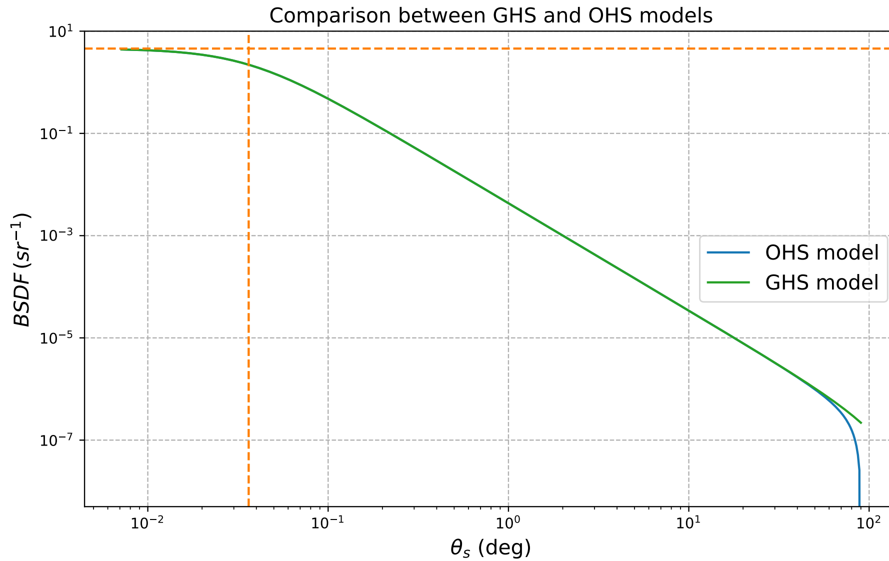

Figure 2.7: Comparison between the derived GHS and OHS models as a function of θ_s. The parameters used for the simulations are the ones used in Fig. 2.6, with the angle of incidence $\theta_i = 0$.

It can be seen that the two models overlap up to about $\theta_s = 50deg$, while at large θ_s there is a notable difference. In particular, while the BSDF derived with the RR approximation tends to zero while θ_s approaches 90deg, the GHS model predicts finite values.

To calculate the TIS, the BRDF model is integrated over one hemisphere. This can be done computationally using the GHS model, integrating numerically in θ from

0 to $\pi/2$ and in ϕ from 0 to 2π. For normal incidence, the TIS can be calculated analytically using the expression:

$$\mathrm{TIS} = \frac{2\pi b}{ls(s+2)}\left[(1+l^2)^{(s+2)/2} - (l^2)^{(s+2)/2}\right], \tag{2.47}$$

where b, l, and s are the fitting parameters of the GHS model.

2.3 Scattering from Particulate

When dust particles are present on the surface of a material, the total scattering is a combination of scattering from surface roughness and light interacting with the particles. Mie scatter theory, named after Gustav Mie, describes scattering by homogeneous, spherical particles. Although dust particles are not typically spherical, it has been demonstrated [18] that assuming all particles are spheres often provides a good approximation of the resulting BSDF.

Mie scattering typically exhibits strong forward scattering, with significant but less intense backward scattering. This results in a distinct pattern with both forward and backward scattering components. The distribution of scattered light is also influenced by the polarization of the light beam.

Consider a spherical and isotropic particle deposited on a surface, with R representing the surface reflectance. The system's geometry is illustrated in Figure 2.8. To compute the total BSDF, two basic assumptions are made. First, particles scatter radiation independently according to Mie's theory. Second, the radiation scattered in the forward direction reflects off the surface without further interaction with the particle.

Therefore, the BRDF results from two components: the light scattered by the particle at a backward-scattering angle θ_b, and the light transmitted through the particle at a forward-scattering angle θ_f, which is then reflected by the surface.

To describe the relation of the intensity and angular distribution of light scattered from a particle, we need to introduce two quantities, the relative refractive index m and a parameter x, given by:

$$x = \frac{\pi Re(N) D}{\lambda} \tag{2.48}$$

where N is the complex refractive index of the particle, D is the particle's diameter, and λ is the wavelength of the incident light.

And m is given by:

$$m = \frac{N}{Re(N_m)} \tag{2.49}$$

where N_m is the refractive index of the media in which the particles are located.

While a comprehensive discussion of the Mie model is beyond the scope of this thesis, detailed information can be found in Mie's original paper [19].

Assuming the incident beam is unpolarized, the BSDF of a surface contaminated with dust particles, given their distribution, is computed as follows:

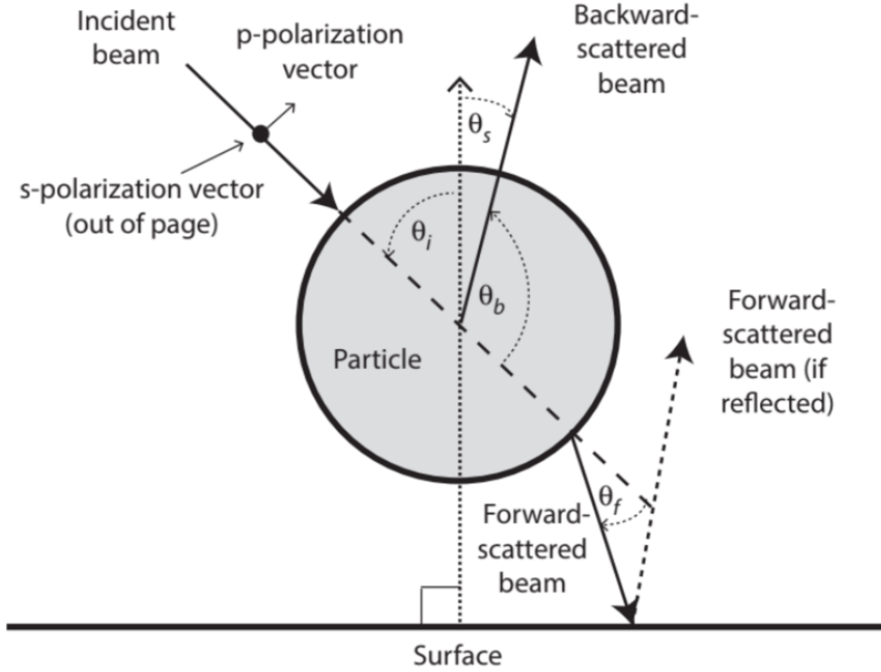

Figure 2.8: geometry of the particle on a surface scattering system (image from [14]). In this case, both the backward- and forward-scattered beams constitute the BSDF.

$$BSDF(\theta_s) = \frac{1}{(2\pi/\lambda)^2 \cos\theta_s} \sum_{i=1}^{N} f(D_i) \times \left[\frac{RI_s(D_i,\theta_f) + RI_p(D_i,\theta_f) + I_s(D_i,\theta_b) + I_p(D_i,\theta_b)}{2} \right] \tag{2.50}$$

where D_i denotes the ith diameter, $f(D_i)$ signifies the particle size distribution function, R denotes the surface reflectance, and $I_s(D_i, \theta)$ and $I_p(D_i, \theta)$ denote the intensities of s-polarized and p-polarized scattered light at the specified scattering angle θ_f and θ_b, respectively.

The λ dependence is particularly important since in general the same dust particle distribution interacting with lasers with different wavelengths may not generate the same amount of stray light. This can be exploited for studying the dimensions of particles in a given medium. When the wavelength of the incident light is comparable to the size of the particles, the shape of the BRDF provides valuable information about the diameter of these contaminants.

When particles are much smaller than the wavelength ($x < 0.1$), Rayleigh scattering provides a more suitable description. This model considers particles as molecules that absorb incoming light by exciting electrons and immediately re-emitting it with the same energy [20]. Rayleigh scattering exhibits a pronounced wavelength dependence, with scattering intensity proportional to $1/\lambda^4$. This implies that shorter wavelengths scatter more intensely than longer ones. In contrast to Mie scattering, Rayleigh scattering produces a symmetric BSDF in forward and

backward directions (and isotropic for p-polarized light specifically) [14], resulting in a more evenly distributed scattered radiation across various angles, as depicted in Fig. 2.9. Rayleigh scattering is also independent of particle diameter.

Geometric scattering occurs when the wavelength of the incident light is larger than the size of the scatterer. In this regime, typically characterized by $D > \lambda$, the scattering pattern exhibits strong forward scattering with minimal scattering in other directions. This phenomenon is prominent in situations where scatterers, such as dust particles or irregular surface features, are significantly larger than the wavelength of the incident light. Geometric scattering patterns can be complex, influenced by the shape and orientation of the scatterer relative to the incident light, and are less dependent on the wavelength compared to Rayleigh and Mie scattering.

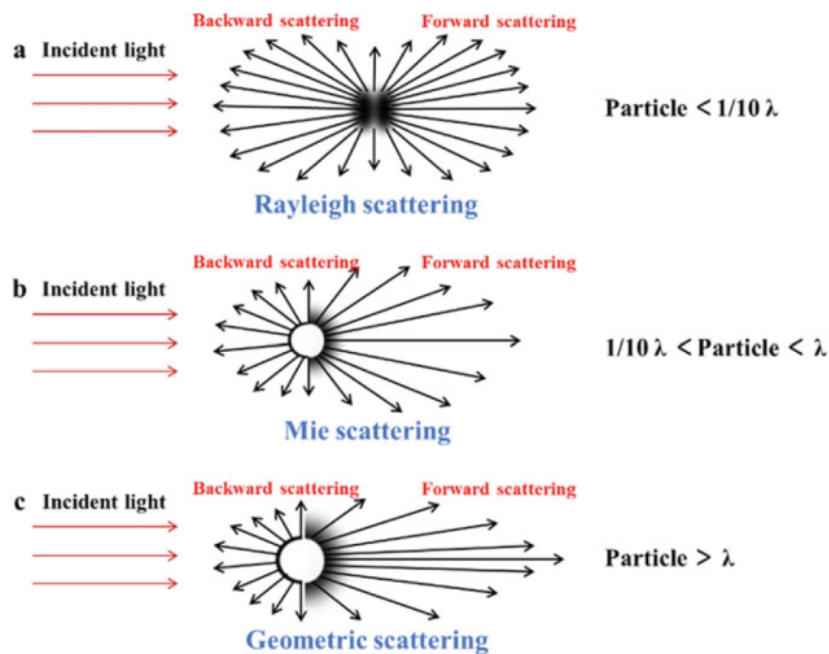

Figure 2.9: Types of light scattering with associated particle diameter ranges relative to the incident light wavelength: (a) Rayleigh scattering, (b) Mie scattering, and (c) geometric scattering. Image from [21].

Chapter 3

Scattering measurement facility

The work carried out for this thesis was conducted in a laboratory at the Dipartimento di Fisica e Astronomia (DFA) of the University of Padua in collaboration with the Istituto Nazionale di Fisica Nucleare (INFN), section of Padua. This laboratory houses the instruments used for the measurements in an ISO-8 clean room, to limit scattering effects from dust on the sample surface, in the air, and on the optics.

On an optical table, a multi-purpose optical setup is constructed, which includes multiple laser lines operating at different wavelengths. The laser paths can be chosen using flip mirrors to redirect the beams to a scatterometer, where they impinge on a sample, and a detector measures the angular distribution of the scattered light. Alternatively, the beam can be directed towards an integrating sphere, which, with the sample mounted inside, measures the total amount of scattered light.

To assist in characterizing the scattering properties of the surfaces, the lab is equipped with a digital microscope with sub-um resolution. Besides allowing visual inspection of the surfaces, the microscope is used to measure the number density function $f(D)$, the quantity used to characterize the scattering from surfaces contaminated by dust, introduced in Eq. 2.50.

In this chapter, I review the main concepts useful for understanding the optical design of the facility, the optical design, and the efforts made to enhance the instrument's sensitivity.

3.1 Optical Setup

The final version of the instrument integrates both the scatterometer and the integrating sphere on the same optic bench, utilizing the same laser sources. The final optical layout is depicted in Fig. 3.3. The entire optical setup is enclosed in a black plastic box with dimensions of 150x90x60cm to shield it from environmental light and dust. Internal panels made of the same plastic separate different sections of the experimental setup. These panels isolate the measurement area, including the detector with the sample mounted, from the area comprising all the optical components to manipulate the beam, where a significant amount of scattered light is generated. The configuration spans two levels on the bench: the first level hosts the source and most of the optics. The integrating sphere is installed at the second

level. The scatterometer structure extends across both levels, with motors and manipulators mainly at the first level and the sample and detector positioned at the height of the second level. The front of the facility is shown in Fig. 3.1.

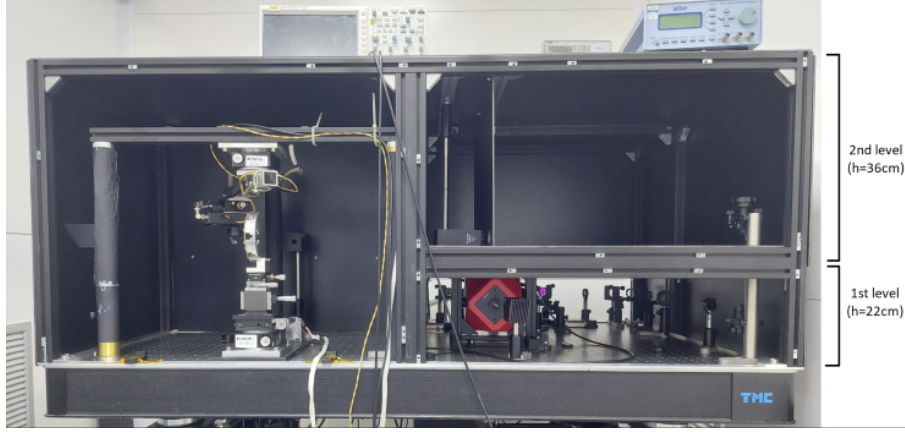

Figure 3.1: Photo of the facility at the current state of June 2024. The area on the left is the scatterometer measurement area that spans between the first and second level, on the bottom-right there is the first level with most of the optics and the integration sphere, temporarily placed there.

The setup includes three light sources, each operating at a different wavelength. Only one laser line can be operative at a time. Specifically, the setup features a 1064 nm laser source, which matches the wavelength used in AdVirgo and other advanced detectors. Additionally, there is a 532 nm green laser source, which is used as an auxiliary laser in AdVirgo and is also of interest for the study of coatings due to its shorter wavelength. Both of these are continuous laser sources and are linearly polarized with a nominal power of 1W. The third light source is a 1550 nm laser, selected as a candidate wavelength for the Einstein Telescope. In the future, a 2000 nm laser, another candidate wavelength for the ET, will be added.

To control the power sent to the sample, a system comprising a half-waveplate (HWP) and a polarizing beamsplitter (PBS) is utilized, shown in Fig.3.2. The HWP rotates the polarization direction of the incident light. The PBS then spatially separates the two orthogonally polarized components: the p-polarization is transmitted, while the s-polarization is reflected. The transmitted component proceeds through the instrument to the sample, while the reflected s-polarized component is diverted 90 degrees and absorbed by a beam dump. By rotating the HWP, the polarization angle is adjusted, thus controlling the power entering the system. The rotating mount of the HWP is motorized (indicated as MHWP in the figure). Additionally, after the PBS, another manually controlled HWP adjusts the polarization of the light beam directed at the samples under study.

Each laser line passes through a telescope consisting of a system of three lenses. The first two lenses are fixed, while the third is mounted on a micrometric translator, allowing adjustment of the beam spot size on the sample. The telescope system is designed based on the principles of Gaussian beam propagation. By moving the third lens, the beam spot size on the sample can be adjusted to range between the orders of 0.1 mm to 2 mm. Using a small spot size allows for higher spatial resolution, enabling

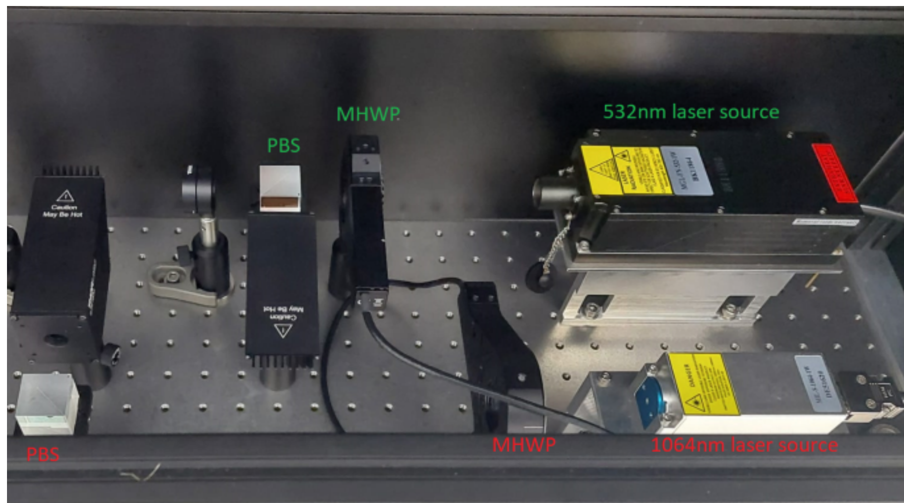

Figure 3.2: Photo of the area where the systems of HWP+PBS are located to control the powers of the 532nm (green text) and 1064nm (red text) laser lines.

finer sampling of the surface. This is important for non-homogeneous samples and in situations where distinguishing surface variations is necessary. Conversely, using a larger spot size provides a measurement of the BSDF averaged over a larger area, thereby reducing the impact of individual imperfections.

The laser beam is then directed either to the scatterometer or the integrating sphere by inserting in or removing from the beam line a few mirrors housed in flip mounts (indicated as "FM" in the figure).

After the 3-lens telescopes which are specific for each line, the different laser lanes share the same paths: either towards the integrating sphere or towards the scatterometer. The laser light is subsequently directed from the first level to the second level using periscopes, which consist of two metal-coated steering mirrors mounted on a vertical structure. In the individual laser lines, both the lenses and mirrors are tailored to their specific wavelengths, with dielectric-coated mirrors used for higher quality at each wavelength. However, in the periscopes, metallic mirrors are necessary to ensure functionality across all three wavelengths used in the instrument. Although this choice results in a slight compromise in quality, it is essential for multi-wavelength compatibility. Depending on the positions of the flip mirrors, the laser beam is sent to either Periscope 1 or Periscope 2, directing it to the integrating sphere or the scatterometer, respectively. For both setups, there are two beam dumps mounted in the directions of the specular reflection and the transmission of the sample to absorb the light and prevent unwanted reflections that could spoil the measurements.

3.1.1 Scatterometer

The instrument used to measure the BSDF of a target sample is the scatterometer. The fundamental components of this device include a laser source, a sample mount, a detector, and beam dumps. The laser beam is directed at the sample, which scatters light. The specularly reflected and the transmitted lights are absorbed by

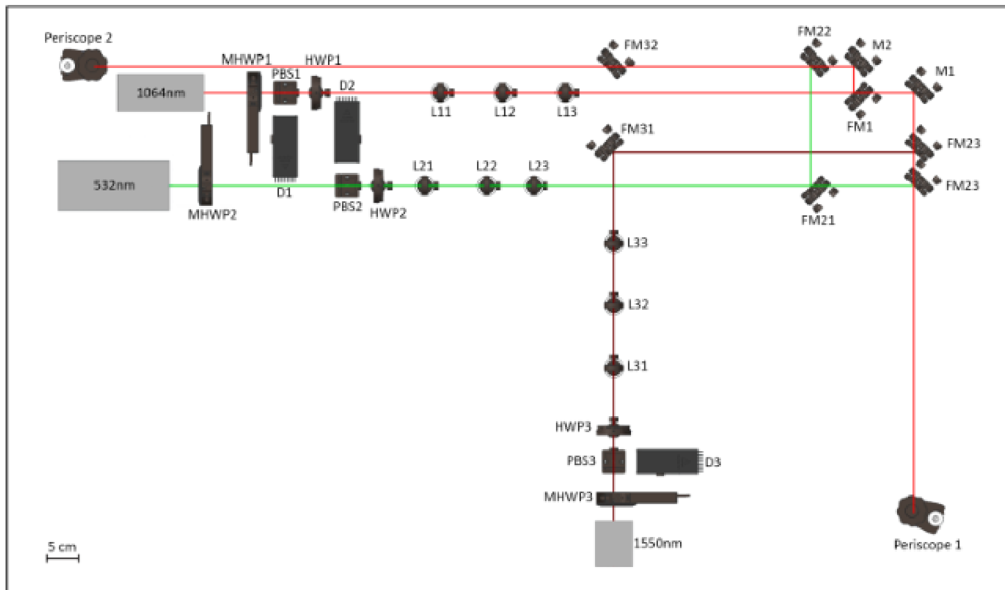

(a) First level.

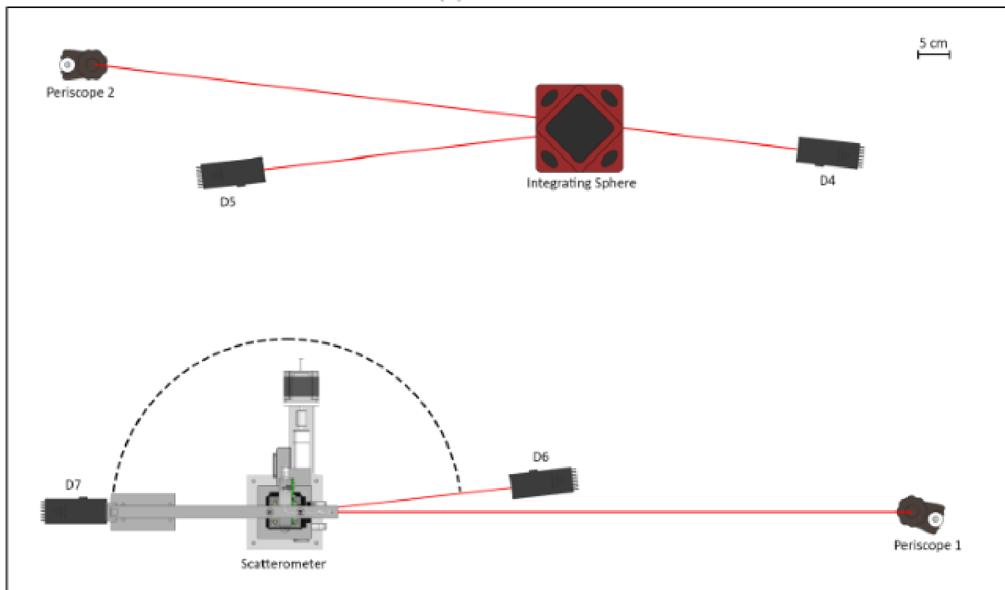

(b) Second level.

Figure 3.3: Target final setup of the instrument. In the figure are shown the two levels of the scattering facility, with all the components described in the text. The green, red, and dark red lines represent respectively the 532nm, 1064nm, and 1550nm laser path. The converged laser path after the flip mirrors is represented in red.

beam dumps, while the remaining scattered light, which is of interest, is captured by a high-sensitivity photodiode that rotates in the incidence plane around the sample at fine angular intervals. This simple setup of the scatterometer is illustrated in Fig. 3.4.

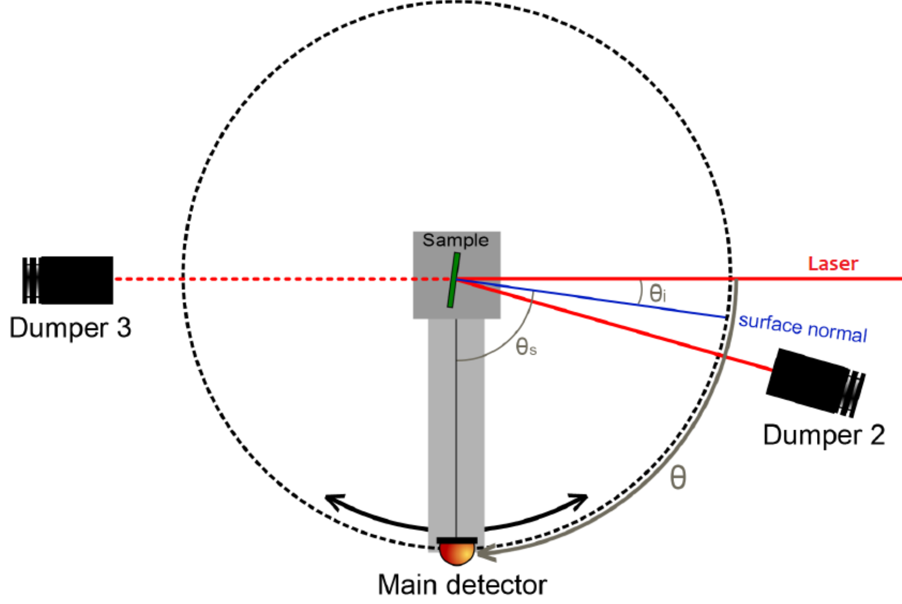

Figure 3.4: Basic setup for a scatterometer showing only the fundamental elements. Image from [22]

The estimation of the BSDF value from a scatterometer measurement at a certain angle θ_s from the surface normal of the sample along the plane of incidence, assuming that the solid angle of the detector is much larger than the solid angle subtended by the laser spot on the sample as seen from the detector, is achieved by applying the Eq. 2.4 to the context of the instrument:

$$BSDF(\theta_i, \theta_s) = \frac{P_s(\theta_i, \theta_s)}{P_0 \cdot \Omega_d \cdot cos(\theta_s)} \tag{3.1}$$

where P_s represents the power scattered by the sample and measured by the detector, P_0 denotes the power incident on the sample's surface, and θ_i is the angle of incidence. The cosine term in the equation accounts for the changing projected surface area of the laser spot on the sample as seen from the detector.

Following the mathematical expression of 3.1, it is evident that at $\theta_s = 90°$, the cosine term becomes zero, and theoretically, also P_s becomes zero because the projected surface area seen by the detector area of the sample is zero. However, what really happens is that some scattering is still measured at this angle due to background contributions. Consequently, the measured BSDF approaches infinity at 90° since the cosine in the denominator becomes zero while the numerator does not. To avoid the non-physical divergence created by this effect, it is common to represent the BSDF multiplied by $cos(\theta_s)$, called cosine corrected BSDF.

Focusing on the scatterometer experimental setup implemented in our scattering facility, to securely hold the sample under study, a sample holder, shown in Fig. 3.5,

with adjustable arms is used to accommodate various sample sizes. The sample holder is mounted on a stack of actuators, providing three translations (x, y, z) and two angular adjustments (yaw and pitch). The rotation of the yaw angle, which determines the incident angle of the laser on the sample, is motorized. All other adjustments are manual. These actuators are used both to align the sample with the laser beam and to align it with the rotation axis of the photodiode.

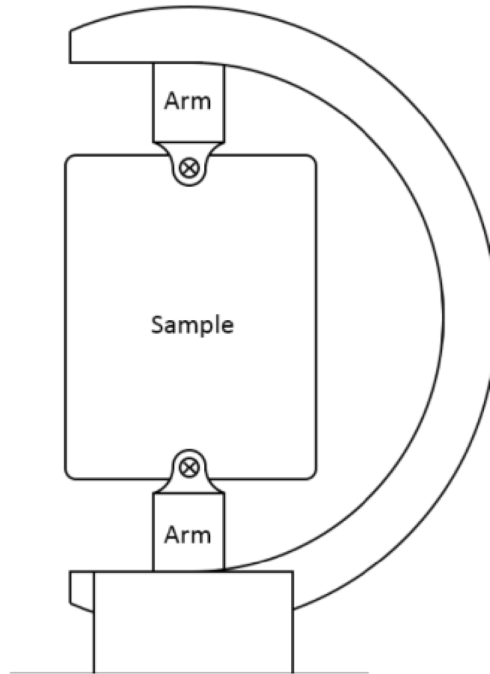

Figure 3.5: Sketch of the sampleholder, the adjustable arms are indicated in the figure and held by circular support. Image from [22].

The photodiode of the scatterometer is supported by a motorized arm that can rotate along a vertical axis which, thanks to the above-mentioned actuators of the sample holder, is made to be parallel and pass through the sample's surface under measurement. Instead of placing the detector directly facing the sample, it is positioned horizontally on top of the arm, with a small prism reflecting the scattered light toward it, as shown in Fig. 3.6. In this configuration, the distance between the sample surface and the photodiode is 25.4 cm. This setup avoids the dead zone caused by the photodiode's housing box, which presents two issues: when too close to the incident beam, it blocks the beam from reaching the sample; and when too close to the reflected beam, it intercepts the beam, generating significant scattered light that can affect the measurement. This allows for measurements at angles closer to specular reflection or direct transmission. The lateral size of the prism is approximately 3 mm (in comparison with the lateral size of 63mm of the photodiode's housing box), enabling measurements at a minimum angle of about 0.3 degrees from the specular reflection, before that mechanical parts of the arm clips with the laser beam. Due to the significant differences in wavelengths among the three laser sources, no single photodiode is sensitive to all wavelengths. Therefore, different photodiodes are required for each wavelength. The New Focus Model 2135 photodiode is used for measuring the 1064 nm light, while the New Focus Model

2151 photodiode is employed for the 532 nm laser light. An iris with a 2 mm diameter aperture is mounted on top of the aperture of both photodiodes. Additionally, filters are used to attenuate the light reaching the photodiode in cases of intense scattered light. For the 1064 nm photodiode, a band-pass filter in the range of [1063, 1065] nm is also applied to select only the relevant portion of the light for the measurements.

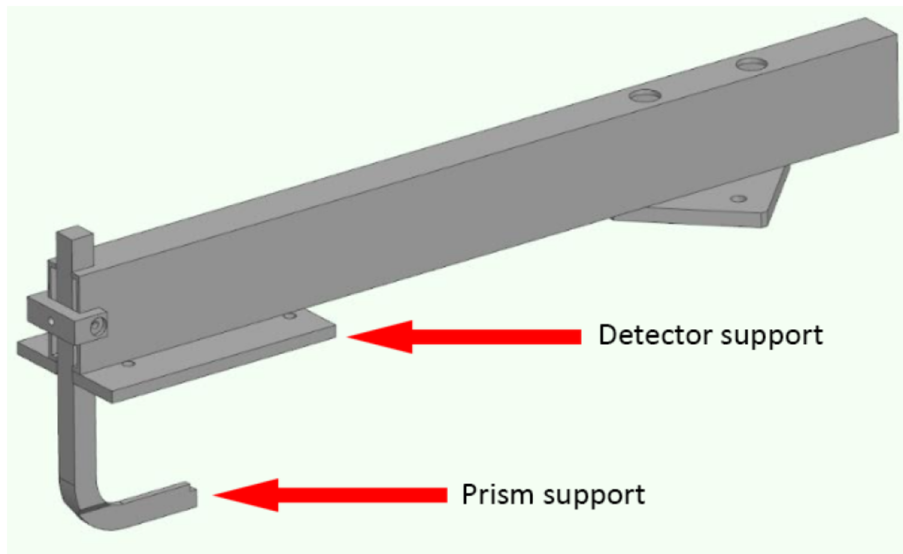

Figure 3.6: Sketch of the rotating arm supporting the detector in horizontal configuration.

To reduce noise, measurements are conducted in AC mode using a Lock-in (LI) amplifier. The laser source is modulated on and off with a 23 Hz square wave generated by a waveform generator. This square wave is also used as the reference input for the LI amplifier. The signal from the scatterometer's photodiode is sent to the input of the LI amplifier. The data is acquired from the output of the LI through an acquisition board connected to a PC.

A custom software was developed specifically for operating the scatterometer. This software controls the motorized components of the setup and manages data acquisition. During measurements, it adjusts the MHWP to control the circulating power in order to have the largest possible signal that does not saturate either the lockin or the photodiode itself. It also moves the photodiode arm to measure the angular distribution of the scattered power, P_s. At the same time, it records the voltage read by the LI output along with the corresponding position where the voltage was acquired.

To transform the recorded output data from LI into a BRDF measurement, the first step in the analysis is converting the LI signal to the corresponding voltage amplitude V_D of the square wave developed at the photodiode:

$$V_D = \frac{V_{LI}}{0.441} \tag{3.2}$$

The coefficient multiplied to V_{LI} is obtained by sending a reference tension to the input of the LI and reading the output value from the output

The next step involves converting the signal from tension to light power. We need to consider the optical elements between the sample surface and our detector, such as the prism and, potentially, filters (in cases where a sample's high BRDF might cause the photodiode to saturate even with the smallest output power). The formula is:

$$P_s = \frac{V_D}{G \cdot R} \cdot F \cdot \frac{1}{R_{prism}} \tag{3.3}$$

Here F denotes the value of the attenuation of the filter used, dependent on the laser wavelength. G and R indicate the gain and the responsivity of the photodiode, respectively. These values can be obtained by the datasheets of the specific photodiode. R_{prism} represents the reflectance of the glass prism.

Then is possible to transform this data into the corresponding BSDF using the formula Eq. 3.1.

In all measurements conducted, I focused primarily on the reflected part of the scattering of BSDF. For the samples studied, the BRDF was the critical parameter, while the BTDF could be safely neglected. This simplification was due to the specific characteristics of the samples, where the transmission component was insignificant compared to the reflection component. Therefore, all reported measurements and analyses are based on BRDF values.

3.1.2 Integrating Sphere

The TIS is defined as the ratio of incident power P_{in} to scattered power P_{scatt}, as expressed in Eq. 2.6. The integrating sphere is used to measure the TIS of a sample by capturing all scattered light within one hemisphere. The integrating sphere, illustrated in Fig. 3.7 (model 4P4 from Thorlabs), can measure both transmitted and reflected scattered radiation, depending on the sample's placement.

The interior of the sphere is composed of a diffusive material, ensuring uniform scattering of any light that strikes it. A photodiode mounted inside the sphere measures the portion of the diffused light that reaches it, converting this light into an electric current. The sphere has three apertures: one for placing the sample, and the other two positioned on the opposite side of the first. These two apertures, depending on the transmission or reflection configuration of the sphere, allow the entry of the impinging laser beam and the exit of the specularly reflected or transmitted beam.

The measurement of the TIS for the hemisphere in reflection, which is correlated with the BRDF, is conducted by placing the sample on the right port as shown in Fig. 3.7. The other two openings are used for the incident beam to enter and the specularly reflected beam to exit, with the laser's angle of incidence on the sample set at 8°. For transmission measurements, which are correlated with the BTDF, the integrating sphere is rotated to allow the laser beam to impinge on the sample, while the transmitted beam exits through the same port used for the specularly reflected beam in the previous case.

Measurements with the integrating sphere are conducted using a reference measurement taken with a diffusive cap. This cap, made of the same material as the

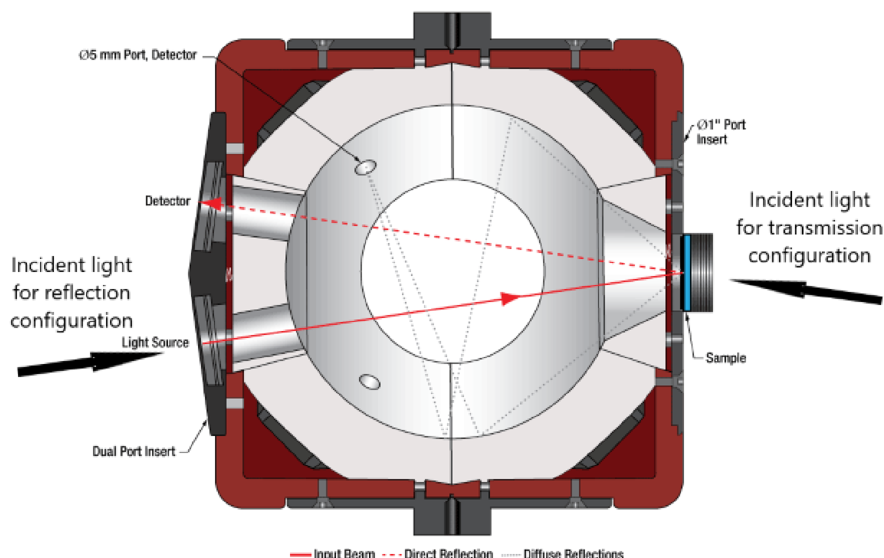

Figure 3.7: Integrating sphere in setup for reflection scatter measurement. Image credit: Thorlabs

sphere's interior, is attached to the opening where the sample is normally placed, fully covering it. In this way, the laser beam that enters is totally scattered, allowing for the measurement of the incoming beam's power P_{in}. Assuming that the TIS of the diffusive cap is equal to 1, all subsequent TIS measurements made with the integrating sphere are normalized to the value obtained with the diffusive cap.

Given the complementary role of the integrating sphere within the scattering facility, I briefly reviewed its functionality for completeness. However, it is important to note that throughout my internship, I did not utilize the integrating sphere. Consequently, it played a marginal role in my work, and I will not delve further into its functionality.

3.2 Current State and Facility Upgrades

When I started my thesis work the stray light facility was still under development: in particular, only the 1064nm laser line was operational. Additionally, optical elements are not yet installed for the 1550nm laser line and instead, the integrating sphere was temporarily mounted in its place to take measurements during the instrument's finalization.

During the period of this work, the ET-Virgo group in Padova made substantial progress on the experimental side, to which I also contributed. One significant change made during my thesis work was the modification of the scatterometer's photodiodes, which impacted the angular range of measurements and the noise floor. Previously, the photodiode was vertically mounted, restricting the scatterometer's measurement range near specular reflection and transmission angles. To avoid clipping the laser beam with the photodiode's body, measurements were limited to angles greater than 13 degrees from specularly reflected and transmitted beams.

With the new horizontal mounting of the photodiode, the range of measurements has been enhanced, allowing measurements up to 0.3 degrees from the reflected and transmitted beams.

Another crucial consideration was the instrument's sensitivity, which was significantly different from the desired noise floor, determined by the scattering of air particles (see Sec. 3.3). Given the complex optical design, unwanted reflections and scattering by the system parts and components could arrive at the photodiode and increase the background light.

3.2.1 Pickup Detector

Another improvement made to the instrument is the installation of a pick-up detector, a photodiode that can detect a sample of the light power after the power control and can be used to monitor the light sent to both the integrating sphere and the scatterometer, for the 1064 nm laser line. This enhancement aims to automate data acquisition and reduce the time required to characterize the sample. As said the custom software controls the light power by maximizing the signal developed at the lockin during the measurement using the motorized half-wave plate; currently, the power output remains constant throughout the measurement.

The installation of pick-up detectors for each laser line was not included in the design shown in Fig. 3.3. For the 1064 nm laser line, we positioned a quasi-transparent window at a small angle of incidence with respect to the propagating beam between the L2 and L3 lenses of the telescope. The slight tilt of the window directs the residual reflected power onto the detector. This new installment is shown in Fig. 3.8.

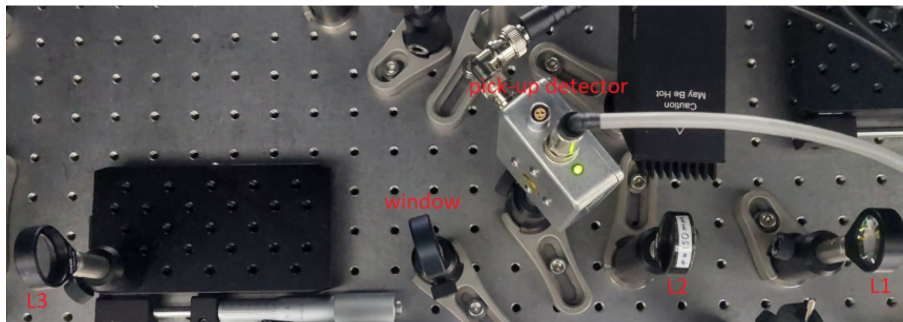

Figure 3.8: Photo of the telescope of the 1064nm laser line with the installation of the quasi-transparent window and the pick-up detector.

To calibrate the pick-up detector, the first step is to measure the (small) reflectivity of the window and estimate the intensity range of the secondary reflection. The pick-up detector is a photodiode connected to a trans-impedance amplifier with an adjustable resistance to fine-tune the output voltage range. This photodiode is connected to the acquisition board, which accepts DC voltage in the range of 0-10V. The power output range of the 1064nm beam reaching the sample is 0.5-800 mW. After testing several resistances, I selected a 560 Ohm resistor that produces 9V at maximum beam power.

Next, I characterized the relationship between the power incident on the pick-up detector and the power generated by the photodiode, and between the power incident on the sample and the voltage generated by the photodiode. This involves using a power meter to measure the power values at the pick-up detector and the sample positions.

By considering a linear relationship between the measured power and the DC voltage output, we can express this relationship as:

$$P = k \cdot V + c \tag{3.4}$$

where P is the power read from the power meter, V is the DC output from the photodiode, and k and c are the coefficients obtained through a linear fit of the data. This calibration is used during the analysis phase to normalize the lock-in signal with respect to the incident power. The plots with the fits are shown in Fig. 3.9

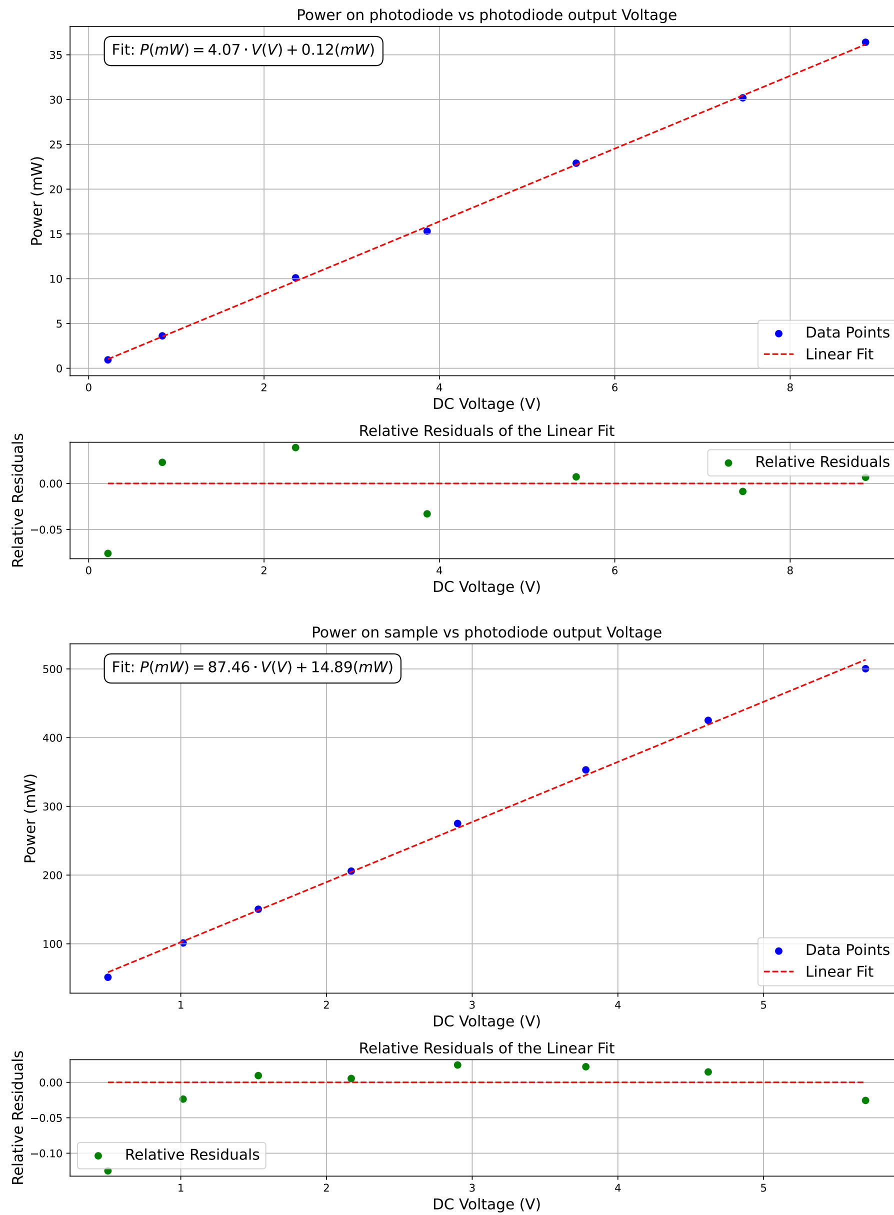

Figure 3.9: Calibration of the photodiode for the 1064 nm laser line. The upper plot shows power measurements on the photodiode with DC output, while the lower plot shows power measurements on the sample with DC output.

The transfer function of the pick-up detector demonstrates a good agreement with a linear response. The non-negligible offsets in the linear fits are attributed to the photodiode generating a small negative voltage even in the absence of incident light, resulting in these minor offsets.

3.3 Scatterometer Background

3.3.1 Theoretical noise floor for BRDF measurements

In general, BRDF measurements made on instruments that measure the scattering, like the scatterometer, are limited by stray light. If not mitigated, the principal sources of stray light can originate from the optical components used within the system or result from internal reflections of light from the surrounding environment. If this type of stray light is minimized within the system, Rayleigh scattering effects may become the primary limiting factor for the measurement of BRDF made on of the system.

As the laser light travels through the air before reaching the sample, it can be scattered by air molecules. Given that the wavelength is much larger than the size of the air particles, this scattering is described by Rayleigh scattering. A formula for the equivalent BRDF due to Rayleigh scattering in gases was derived in [23], with a corrigendum [24]. Using these works and following the derivation and calculations performed in [22] for a previous version of our instrument, we can estimate the air scattering contribution to the BRDF measurements.

The geometry of the setup is illustrated in Fig. 3.10. The light beam travels along the z-axis and has a cross-section A_d. The detector is located at point p, which is at an angle η_0 (denoted as θ_d in this text) from the z-axis, and has an area A_p. The distance from the detector to the rotation center point O, at $z = 0$, around the sample is r_0, which in our scatterometer is $0.254m$. The length of the beam within the detector's field of view is l.

To make the quantity l explicit, the detector's field of view is defined as the angular aperture and, for simplification of later calculations, it is set as $FOV = 2\gamma$. The total value of l can then be calculated by summing the components l_1 and l_2, derived from the trigonometric relations of the triangles shown in Fig. 3.11:

$$l_1 = r_0 \frac{sin\gamma}{sin(\gamma + \theta_d)} \qquad l_2 = r_0 \frac{sin\gamma}{sin(\theta_d - \gamma)} \tag{3.5}$$

With the assumption of $\gamma \ll 1$ (as a consenquence, it also means $l \ll r_0$), l results in:

$$l_1 = l_2 = l/2 = r_0 \frac{\gamma}{sin(\theta_d)} \tag{3.6}$$

The equivalent BRDF scattered by the air f_{air} is calculated using a reference sample with a known BRDF, f_R. The calculation is based on the principle that the ratio of the BRDFs is equal to the ratio of the average scattered fluxes of the reference sample and the air. This relationship can be expressed as:

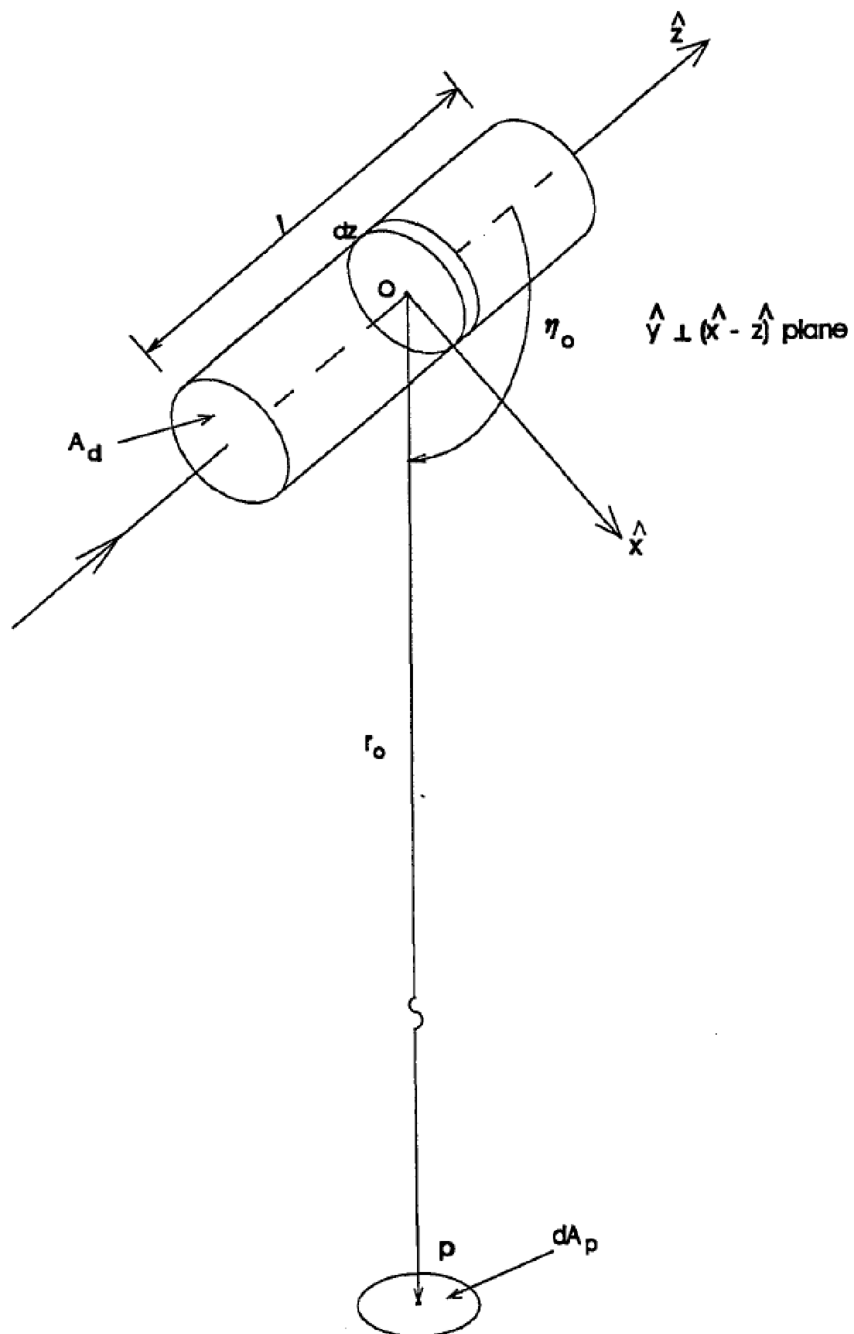

Figure 3.10: Geometry of the problem. Credit: [23].

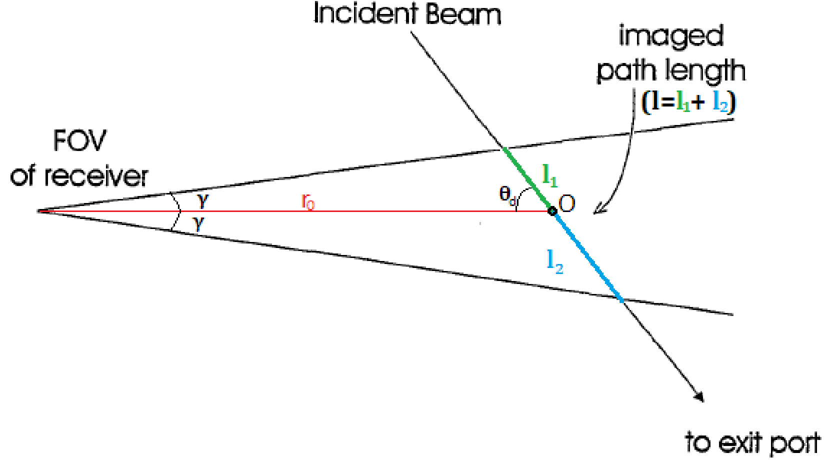

Figure 3.11: The lengths l_1, l_2 and the angles θ_d and γ as indicated in this text.

$$\frac{f_R cos\theta_s}{f_{air}} = \frac{\Phi_R}{\Phi_{air}} \tag{3.7}$$

Here Φ_R is the scattered flux of the reference sample, and Φ_{air} is the scattered flux of the air. The term $cos\theta_s$, which accounts for the change in the projected area, is applied only to the reference sample. This is because air scattering, described by Rayleigh scattering, is uniform across all θ_s.

Starting from the scattered flux Φ_R, in the absence of air molecules (i.e., in a vacuum), the flux detected when a sample characterized by f_R is exposed to an average irradiance given by the incident flux Φ_I divided by the irradiated area, as explicated in 2.3, is:

$$\Phi_R = f_R \Phi_I \Omega cos\theta_s \tag{3.8}$$

where Ω is the solid angle of the detector, given by A_p/r_0^2, assuming the dimension of the detector is small compared to the distance of the detector $A_p \ll r_0^2$.

To obtain the flux generated by air Φ_{air}, we start from the scattered irradiance E'_p at point p of one molecule using Rayleigh scattering theory [23]:

$$E'_p = \frac{k^4|\alpha|^2}{r^2} E_i \tag{3.9}$$

where k is the wave number ($k = 2\pi/\lambda$ with λ being the wavelength of light), α is the polarizability of the gas ($\alpha = [3/(4\pi N)][(n^2-1)/(n^2+2)]$, where n is the index of refraction of the gas, which is 1.0003 for air, and N the average number of gas molecules per unit volume), E_i is the irradiance of the light beam on the cross-section A_d. Consequently, the number of gas molecules contained in a section of volume $A_d dz$ is $A_d dz N$. Considering A_d with a radius much smaller than r_0, the irradiance E_p at p caused by the scattering of all the gas molecules in volume A_d can be written as:

$$E_p = \int_{l/2}^{-l/2} A_d N E_p' \, dz = \frac{A_d}{r_0^2} N k^4 |\alpha|^2 E_i L \tag{3.10}$$

with:

$$L = r_0^2 \int_{l/2}^{-l/2} \frac{1}{r^2} \, dz \tag{3.11}$$

Here r is the distance between p and any location along z within l, and it is defined as

$$r^2 = r_0^2 + z^2 - 2r_0 z cos\theta_d \tag{3.12}$$

E_p can be expressed as Φ_{air}/A_p, and E_i can be written as Φ_I/A_d. Thus, Eq. 3.10 becomes:

$$\Phi_{air} = \frac{A_p}{r_0^2} N k^4 |\alpha|^2 \Phi_I L \tag{3.13}$$

Plugging Eq. 3.13 and Eq. 3.8 into the right-hand side of Eq. 3.7, and using $\Omega = A_p/r_0^2$, we have:

$$\frac{f_R cos\theta_s}{f_{air}} = \frac{f_R cos\theta_s}{N k^4 |\alpha|^2 L} \tag{3.14}$$

resulting in:

$$f_{air} = N k^4 |\alpha|^2 L \tag{3.15}$$

In the case of $l \ll r_0$, we can approximate $r^2 \approx r_0^2$, resulting in $L = l$. In this case the BRDF results:

$$f_{air} = l N k^4 |\alpha|^2 \tag{3.16}$$

As concluded by Asmail et al. (1999), this assumption may not be precise for our specific photodiode. The iris, with a 2 mm aperture, is mounted approximately 2 cm from the photodiode's aperture, resulting in a non-negligible FOV of 11.4°. When the detector is positioned at 90° relative to the incident beam (minimum value of l), we have $l \sim 0.026m$. This represents approximately 10% of r_0. Therefore, to get a precise estimation of f_{air} I employ the full integral form. For the calculation without the approximation of L made in 3.16, I will follow the derivation made in [22].

Starting from the limits of integration in Eq. 3.10, they are also derived under the assumption that l is very small, allowing to symmetrically consider half of l on either side of the z-axis, as derived in Eq. 3.6. In our case, these limits are not symmetrically applicable. Therefore, instead of integrating from $-l/2$ to $l/2$, we divide l into the two segments l_1 and l_2 described in Eq. 3.5, representing the lengths on the positive and negative sides of the z-axis, respectively. The integration is then performed from $-l_2$ to l_1.

In this way, we have parametrized L as a function of θ_d:

$$L(\theta_d) = r_0^2 \int_{-r_0 \frac{sin\gamma}{sin(\gamma-\theta_d)}}^{r_0 \frac{sin\gamma}{sin(\gamma+\theta_d)}} \frac{1}{r^2}\, dz \tag{3.17}$$

The interval of θ_d of our interest (for non-transparent samples) to simulate f_{air} is in the order of $[0°, 90°]$, but for completeness, we will cover the entire interval of the order of $[0°, 180°]$. Before estimating the value of $L(\theta_d)$ in this interval we need to deal with two singularities of the integral. The first one is on the limits l_1 and l_2; as θ approaches $\pi - \gamma$ and γ, respectively, l_1 and l_2 tends to infinity, and thus does l. In practice, this is prevented by the beam being absorbed by a dumper positioned at $d \gtrsim r_0$ from the detector's rotation center. The second issue arises when $\theta = 0$ or π. In this case, the term $1/r^2$, for the definition of r in Eq. 3.12, in L diverges. However, the Eq. 3.12 is invalid for very small distances, and in our case, since our photodiode never approaches such small angles to prevent unintended scattering with the mechanical parts of the scatterometer, these angles are out of our interest.

The first problem is resolved by setting a maximum value for l_1 and l_2 equals to r_0. The second problem can be resolved by limiting the interval where varying θ in $[\theta_1, \theta_2]$ with $\theta_1 \gtrsim \gamma$ and $\theta_2 \lesssim \pi - \gamma$. Considering that in our case $\gamma = 5.74°$, the selected interval of θ_d is $[6, 174]$. This interval adequately covers the measurement range.

The full integral form of Eq. 3.11 cannot be easily solved analytically. Therefore, numerical methods were employed to integrate the function. N can be estimated using the ideal gas law, assuming a pressure of $1atm$ and a temperature of $300K$, which gives $N = 2.45 \times 10^{25} m^{-3}$. These calculations are performed for the three wavelength sources of the instrument, which are $532nm$, $1064nm$, and $1550nm$. In Fig. 3.12 are shown the simulation of f_{air} as a function of the angle θ_d within the range of $\theta_d = [6, 174]$.

In the next section will be shown the comparison between the simulated and the measured BRDF from air scattering for the $1064nm$ laser.

3.3.2 Scatterometer Background Optimization

My primary focus during my work on the scatterometer was to enhance its sensitivity to approach the air BRDF noise floor. A significant effort was dedicated to investigating internal stray light within the scatterometer. Given the high power of the laser sources relative to the sensitivity of the measurements, even minimal scattering could potentially affect the accuracy of the readings. Quantifying the maximum orders of magnitude difference that we can expect to measure with our instrument between the power circulating in the laser line P_{in} and power scattered by the sample P_s, considering that the scatterometer can measure up to BRDF$\sim 10^{-9}$ and calculating the value of $\Omega_d \sim 10^{-5}$, by Eq. 3.1 the minimum ratio P_s/P_{in} results in $\sim 10^{-4} \times cos\theta_s$.

To assess the scatterometer's sensitivity, I utilized the 1064nm laser line, which was operational at the time. Although each laser line is initially different, they eventually converge onto the same path, allowing most analyses to be conducted using a single laser line.

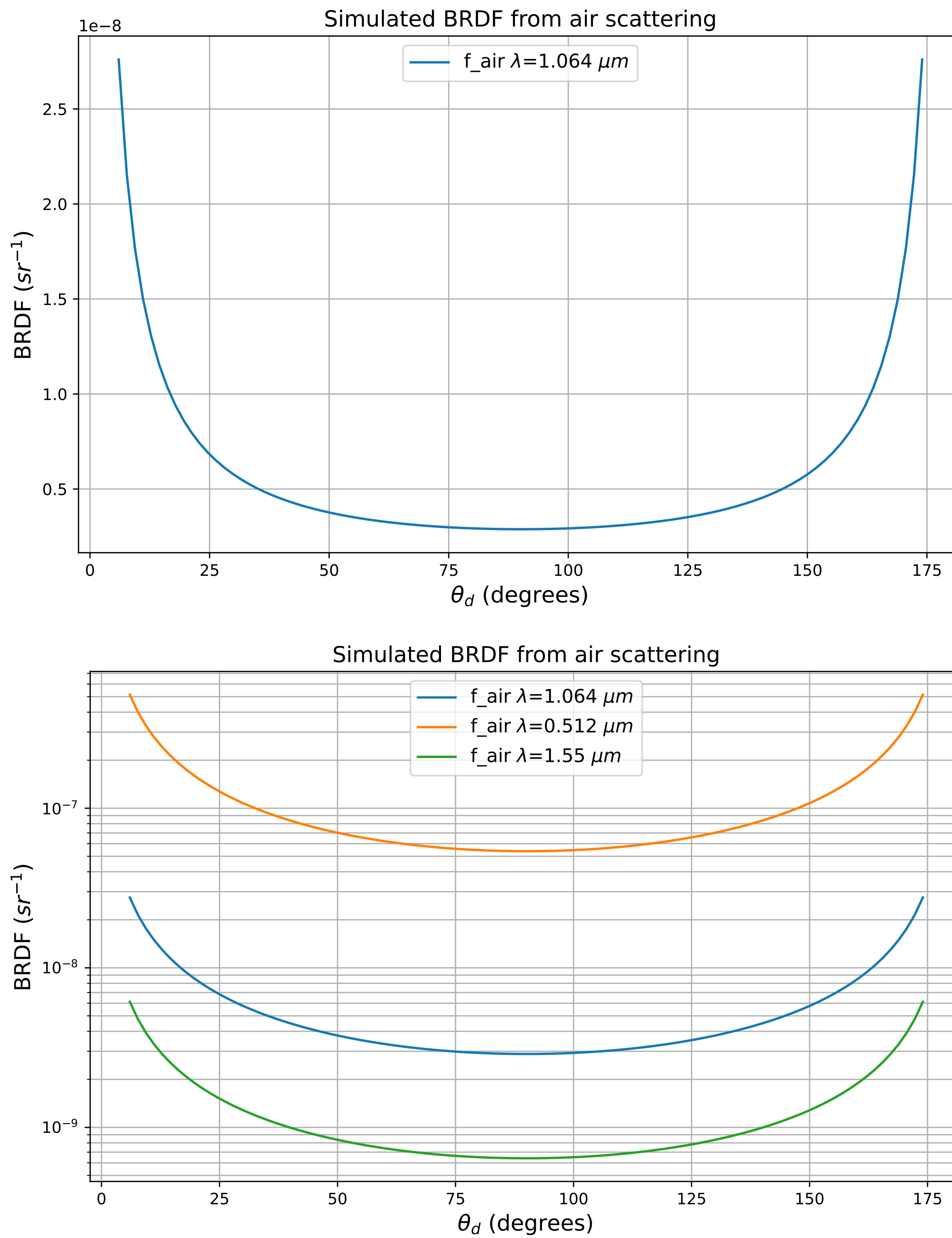

Figure 3.12: Simulations of air scattering BRDF. The first plot shows the BRDF simulation at 1064 nm in linear, while the second plot presents BRDF simulations at 532 nm, 1064 nm, and 1550 nm in logarithmic scale given the wide spread of amplitudes. Both plots cover the angular range of θ_d from 6 to 174 degrees.

To evaluate the instrument's sensitivity, measurements were conducted without the sample holder, directing the laser directly to the transmission dumper. This type of measurement is referred to as a background measurement. However, it is important to note that the background may differ in actual measurements for at least two reasons: firstly, the primary beam follows a different path when the sample is reflective; and secondly, there might be contributions from light scattered by the sample in directions other than θ_s, which could then bounce off some part of the setup and eventually reach the detector. Maximum power was applied to maximize the light power detected by the scatterometer's photodiode in order to better measure the noise floor due to the air scattering and any unwanted extra contributions. A typical background measurement performed at the beginning of my work is shown in Fig. 3.13: several features and peaks are visible that are orders of magnitude higher than the air scattering limit.

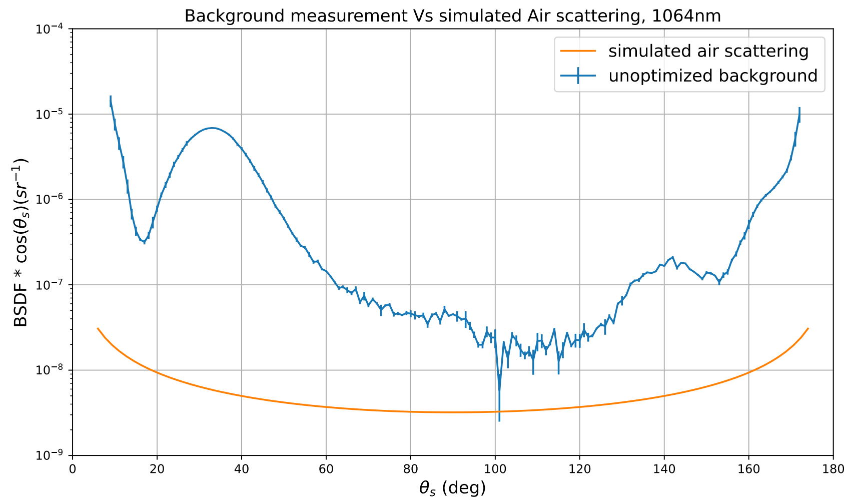

Figure 3.13: Example of one of the first background measurements. Here can be noted multiple features of the measure that can be explained as straylight.

Considering the variations in shape and symmetry of the bumps observed in the background measurements, as in Fig. 3.13, it was evident that multiple sources of background light (either as scattered light and/or ghost beams) were present This necessitated a comprehensive investigation of these sources. The strategy employed involved systematically moving, tilting, adding, or removing various mechanical and optical components, one at a time, and measuring the resulting background to isolate the sources of stray light.

The major contributor to the background noise was identified as the external body of the transmission dumper. Although the laser beam fits the dumper entrance, a halo of diffuse light originating from the region around the sources re-enters the laser path, reaches the measurement area, and impinges on the outer body of the dumper, causing scattering. Secondary diffuse reflections from panels of the surrounding black box resulted in stray light reaching the photodiode during measurements, creating significant bumps and features, the most important being the one in the range of θ_s $[20-40]$. In Fig 3.14, the variation of the background can be observed as the dumper is moved or tilted. It is important to note that in each

new position, the laser beam continues to enter the dumper.

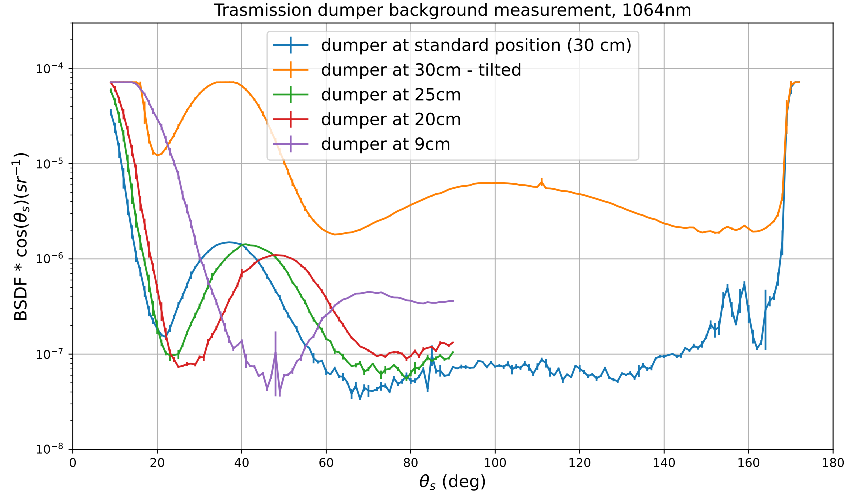

Figure 3.14: Study of the resulting background moving and tiling the transmission dumper. This plot shows how the background depends on the position of the dumper.

The issue was resolved by adding two irises. One iris was placed on the first level of the instrument between the flip mirrors and Periscope 1, and the other was positioned between Periscope 1 and the sample. This effectively mitigated the problem. The irises were adjusted to let the beam's waist at their respective positions widely go through the irises while cutting off the problematic halo.

To minimize the remaining sources of diffused light background noise, additional minor adjustments were made. The legs supporting the motor and the arm of the photodiode were covered with black aluminum foil. One of the internal panels that isolated the scatterometer's measurement area was cut in half primarily to better position the reflection dumper. This allowed the reflected beam to be safely dumped at small incident angles θ_i and also enabled the upper part of the panel to be repositioned to reduce scattering.

The final background for the 1064 nm laser line is shown in Fig. 3.15. The electronic noise of the instrument is also plotted, showing that the noise floor is comparable to the electronic noise. This indicates that the sensitivity of the instrument is limited by both air scattering and the inherent limitations of the photodiode used for the measurements. Compared to the initial unoptimized background, the final background demonstrates significant improvements, lowering the background down to the air scattering limit.

The measured background aligns with the expected BRDF estimated from air scattering within the interval of θ_s $[10-50]$. In other parts of the measured interval, the background is slightly higher but does not exhibit significant bumps or other features. Given the initial target sensitivity at the beginning of the optimization process was to achieve a sensitivity on the order of $\lesssim 10^{-8} sr^{-1}$, the results successfully met this goal.

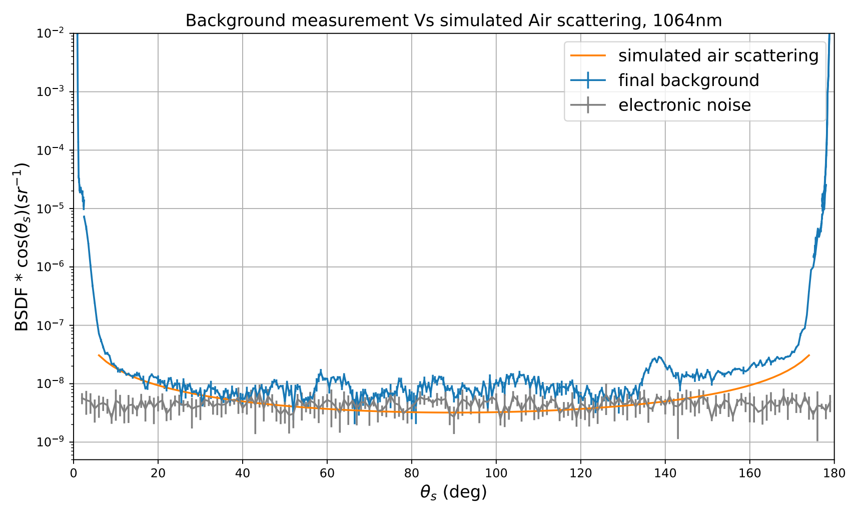

Figure 3.15: Final background measurement.

Chapter 4

Measurements

After optimizing the background of the scatterometer, the instrument is now capable of taking precise measurements of the BRDF of a sample. Two different groups of samples are analyzed with the scatterometer: samples with scattering from surface roughness, and samples contaminated by dust with scattering dominated by the dust deposited. The interested scattering of these samples is the reflected part, so the BRDF measurement is conducted over the reflected hemisphere, spanning the interval of θ_s from 0 to 90 degrees.

A standardized procedure is followed for measuring a sample. The sample is mounted on its holder (as shown in Fig. 3.5), and a motorized stage allows for precise rotation to set the angle of incidence, θ_i, of the laser impinging on the surface. The angle θ_i chosen for all the measurements is 3.8 deg, which is the lowest angle of incidence while the specularly reflected beam is safely dampened. The photodiode, mounted on another motorized stage, rotates around the sample and measures the BRDF at arbitrary intervals. At each point, the photodiode takes five measurements, and the final data is the average of these measurements, with the associated error given by the standard deviation. Each sample is impinged by the laser in only one spot which is approximately in the center of the sample-holder. The plots showing on the y-axis the values of the cosine corrected BRDF are typically displayed as a function $|sin(\theta_s) - sin(\theta_i)|$. In the case of this setup with θ_i, the range of the x-axis is [0,0.93].

The full scale of the photodiode used for measurements is optimized to detect the power of scattered light at larger angles, which is significantly lower compared to the power around the specularly reflected beam. Even with filters mounted on the photodiode to reduce power, angles near the specularly reflected beam must be avoided to prevent saturation or damage to the photodiode. Given that all measurements are taken with θ_i of 3.8 degrees, placing the specularly reflected beam at $\theta_s = 3.8$ degrees, the measurement interval for θ_s typically starts between 5 and 7 degrees, depending on the reflective properties of the sample, and extends up to 90 degrees. Additionally, care must be taken to ensure that the power scattered, in particular at large scattering angles of θ_s where the scattering reaches very low levels, does not fall below the electronic noise of the photodiode. For this reason, in particular for the surface roughness ones, due to the significant variation in scattered power over the entire measurement interval, the BRDF measurement of a surface

is performed through a composition of measurements with complementary intervals at different incident power levels on the sample. However, because this process requires considerable time, it limited the number of measurements I was able to take, resulting in fewer measurements than desired. For improved statistical reliability, each sample should be characterized by the scatterometer with the laser impinging on different points of its surface.

4.1 Scattering from surface roughness

For samples characterized by the scatterometer to measure scattering from surface roughness, in addition to the information on the angular distribution of the scatter, the BRDF$\cdot\cos(\theta_s)$ measurements can be used to determine the RMS surface roughness. The following section provides a detailed analysis of the data processing procedure used to extract this information from the measurements.

4.1.1 Effective RMS Roughness

When probing a surface to study its surface roughness using a laser beam characterized by a wavelength λ, it is important to note that spatial frequency components of the surface profile greater than $1/\lambda$ do not contribute to optical scatter. Therefore, the total effective RMS surface roughness must be considered, defined as [14]:

$$\sigma_\lambda = \left\{ \int_{1/d}^{1/\lambda} S_2(f)df \right\}^{1/2} \tag{4.1}$$

where d is the spatial extent of the beam used to measure the integral of S_2. Consequently, the scatterometer can only recover a band-limited version of the RMS surface roughness described in Eq. 2.9.

To obtain the effective RMS roughness σ_λ from BRDF$\cdot cos(\theta_s)$ measurements, it is necessary to calculate the TIS using Eq. 2.5. Given that smoothly polished optics should scatter isotropically, we can assume that the BRDF function is independent of azimuthal scattering angles ϕ_s, so the integration is then performed:

$$TIS = 2\pi \int_0^{\pi/2} BRDF(\theta_s) cos\theta_s \, sin\theta_s \, d\theta_s \tag{4.2}$$

Using the formula presented in [14], the effective RMS roughness of the surface can be determined:

$$TIS = \left[\frac{2\pi \Delta n \sigma_\lambda cos\theta_i}{\lambda} \right]^2 \tag{4.3}$$

rearranging the previous equation, the effective RMS surface roughness is equal to:

$$\sigma_\lambda = \frac{\lambda \sqrt{TIS}}{2\pi \Delta n cos\theta_i} \tag{4.4}$$

Due to the incompleteness of the experimental data over the entire interval of θ_s of [0,90]deg, a fit to the data, which has been renormalized with $cos(\theta_s)$, is performed using the GHS model approximated for smooth surfaces of Eq. 2.46. This fit yields the parameters b_0, l, and s. Using these fitted parameters, the BRDF is then calculated over the interval of θ_s [0,90]deg, covering the scattered hemisphere.

It is important to note that due to the nature of the BRDF, while the slope parameter s is derived from points measured at large scattering angles, the data points near the specular reflection are crucial for obtaining precise values of the fit parameters b_0 and l. As noted previously, these near-specular angles are challenging to measure. Alternatively, if the data points are insufficient to determine the parameters b_0 and l, or if the model used does not accurately represent the data trend, the TIS calculation is performed directly on the measured data using the formula:

$$TIS = 2\pi \int_{\theta_1}^{\theta_2} BRDF(\theta_s) cos\theta_s \, sin\theta_s \, d\theta_s \tag{4.5}$$

The integral calculated in this equation is called the optical loss of the surface and represents the fraction of the light power scattered away due to surface roughness in the range of $[\theta_1, \theta_2]$. It is a fraction of the total TIS and using it to calculate the effective roughness σ_λ will of course yield a lower limit of the actual value. For our samples, about 7 degrees of the total interval are lost. Although this might seem minimal, it includes the reflected peak, which contains the highest values of the function. Nonetheless, the result obtained in this manner provides important information on the real effective RMS roughness's order of magnitude.

4.1.2 CERN steel samples

The first samples studied with the scatterometer consist of three different types of stainless steel received from CERN laboratories. CERN is actively involved in the design and realization of the Einstein Telescope, specifically focusing on the selection of materials for the beampipes. The stainless steel samples, categorized as austenitic, ferritic, and mild, vary in composition and manufacturing processes, which results in different surface roughness properties. As can be noted in Fig. 4.1, the surface of these samples shows anisotropic features. The steel samples do not undergo typical manufacturing methods assumed in Eq. 2.15, and their surface profiles cannot be approximated using the K-correlation model, so the data cannot be fitted with the derived GHS model.

As a result, in this case, the scatterometer is not suitable for studying their roughness directly. Instead, the surface roughness is measured independently using the digital microscope and a profilometer, enabling the measurement of the surface roughness. Due to the anisotropic surface pattern of the samples, it is also not possible to calculate the TIS using Eq. 4.5, which assumes isotropic scattering in azimuthal angles for its validity. The only information on these samples that can be extracted using the scatterometer is the angular behavior of the scattered light, shown by the plot of BRDF $\cdot\, cos(\theta_s)$ within the studied interval.

The ferritic sample exhibits a distinct surface texture characterized by a pattern of parallel lines, which is particularly evident in the magnified microscope image in

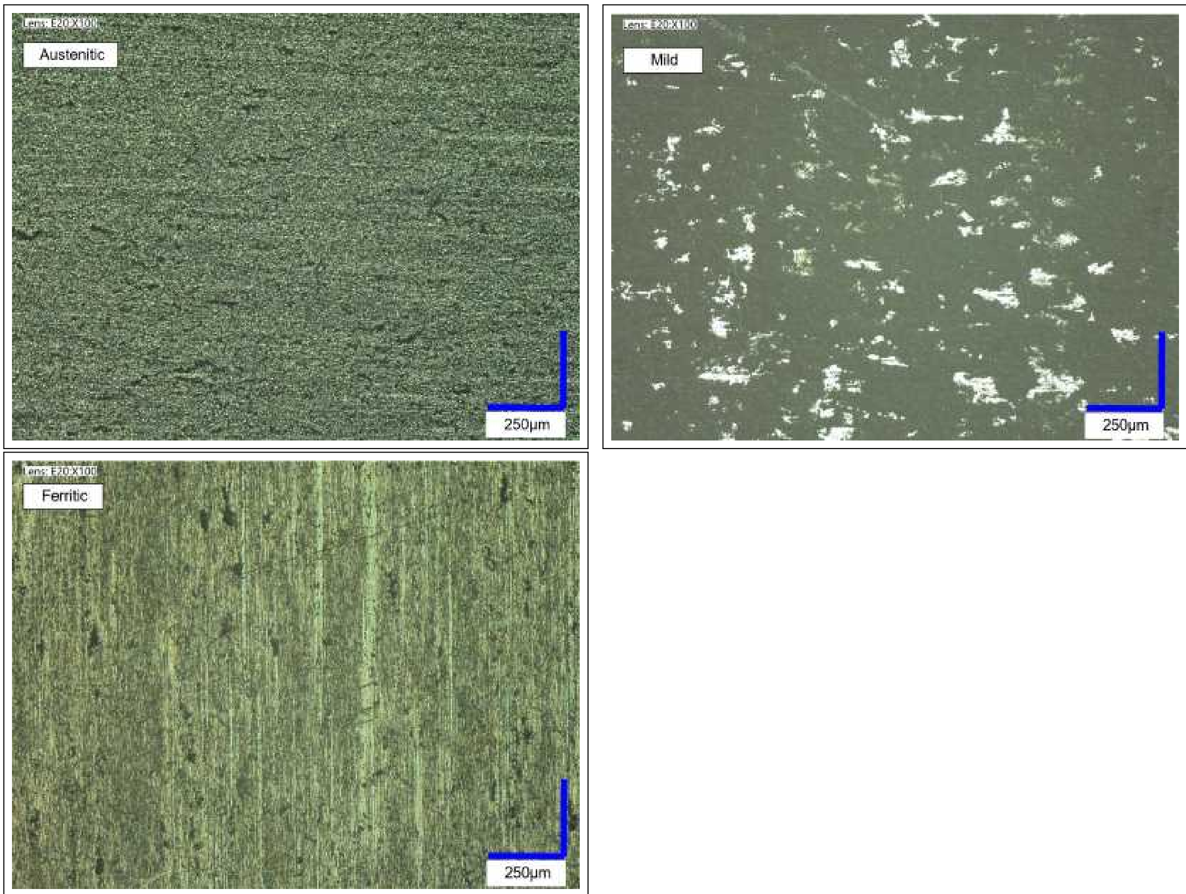

Figure 4.1: Images of the CERN steel sample using the digital microscope at x100 magnification. They are: Austenitic top-left, Mild top-right, Ferritic bottom-left. They all show anisotropic features on the surface, particularly the ferritic sample. Image from [25].

Fig. 4.1. For this sample, the BRDF is measured along two perpendicular directions relative to the pattern lines.

The measurements are done with the 1064nm laser line and the results of the measurements are displayed in Fig. 4.2. Due to the high power of the scattered light, we had to use a filter, with an optical density (OD) of 2.81, mounted to the photodiode over the entire range of measurements. Despite also using the minimum power, around half of a milliwatt, the photodiode saturates up to the θ_s of 15 deg in the case of the ferritic sample.

It is observed that the orientation of the ferritic sample's surface pattern significantly influences the amount of scattering. When the pattern is positioned vertically, the scattered power is an order of magnitude greater than when the pattern is positioned horizontally.

The austenitic steel sample, similar to the ferritic sample, exhibits a decreasing trend in scattering intensity as a function of θ_s. The difference in scattering intensity between small and high values of θ_s spans approximately three orders of magnitude.

The mild steel sample behaves as a Lambertian scatterer, with a plateau observed in the measured data within the interval of $|sin(\theta_s) - sin(\theta_i)|$ [0.1, 0.8]. Due to the small dependence of θ_s, the scattering intensity of this sample is the lowest at a

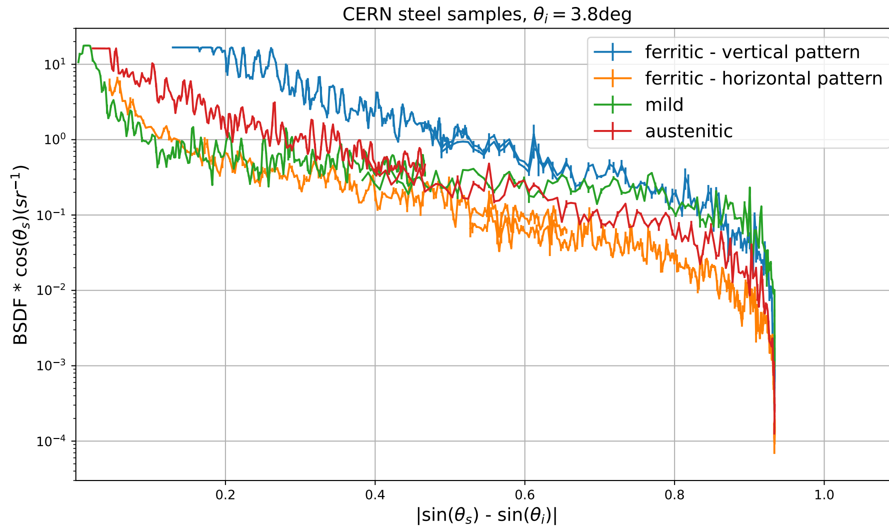

Figure 4.2: Plot of measured BRDF $\cdot \, cos(\theta_s)$ data of the CERN steel samples as a function of $|sin(\theta_s) - sin(\theta_i)|$.

small θ_s and becomes the highest at a high θ_s compared to the other types of steels which display a continuously decreasing scattering behavior with increasing.

4.1.3 Baffles samples

Another type of samples studied with the scatterometer are stainless steel samples provided by IFAE and coated by Optimask (Paris), which have a Cr/Cr_2O_3 2-layer anti-reflective coating. These materials are used for the stray-light baffles in the Virgo interferometer. There are two types of samples, labeled 68B and 69B. Both samples are double-sided, with one side featuring a uniform texture across the entire surface, referred to as “uniform.” The other side has a stripe with a different texture on the bottom, referred to as “non-uniform”. We do not have information on why the two surfaces are different or which one is representative.

Each surface is studied using the scatterometer, and for the non-uniform samples, it is avoided to impinge with the laser on the stripes during the scattering measurements. The measurements are conducted using the 1064 nm laser line. To prevent saturation, the same filter with an OD of 2.81 is used near specular angles, with the first θ_s measured at 6 degrees. The plot of the data is shown in Fig. 4.3. Initial observations indicate that the surfaces of the non-uniform samples exhibit higher scattering and different, less regular behavior compared to the uniform samples, particularly for the 69B non-uniform sample.

The data points are fitted using the GHS model described in Eq. 2.46 for polished smooth surfaces. The plot of the renormalized BRDF fitted with the GHS model for every data set is shown in Fig. 4.4. The fits show good agreement with the data points of the uniform samples, whereas, for the non-uniform samples, there is not good agreement with the experimental data, suggesting the presence of additional scattering mechanisms in these samples. The fitting parameters for the uniform samples are displayed in Table 4.1.

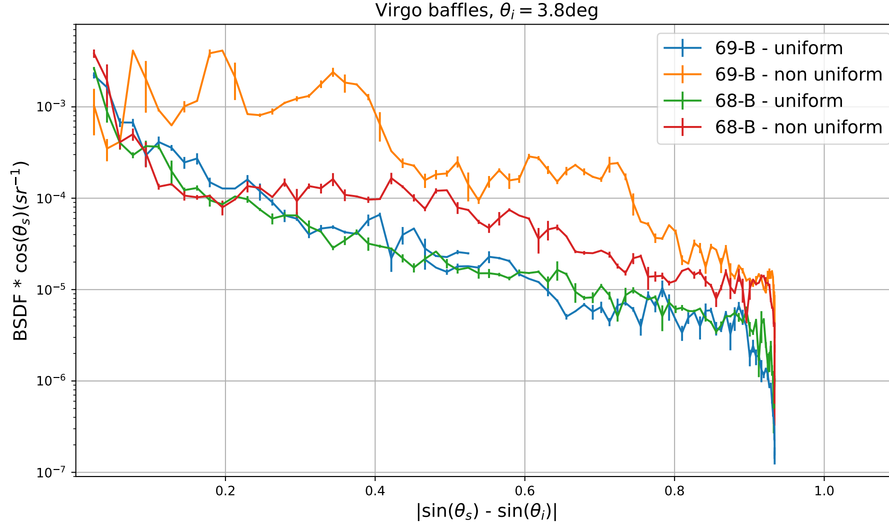

Figure 4.3: Plot of measured BRDF $\cdot$ $cos(\theta_s)$ data of the baffle samples as a function of $|sin(\theta_s) - sin(\theta_i)|$.

Sample	b_0 (sr^{-1})	l	s
68B-u	$(145 \pm 17) \cdot 10^{-6}$	$(90 \pm 18) \cdot 10^{-3}$	-1.75 ± 0.20
69B-u	$(274 \pm 34) \cdot 10^{-6}$	$(75 \pm 14) \cdot 10^{-3}$	-1.82 ± 0.18

Table 4.1: Results of the parameters b_0, l and s of the GHS fit on the uniform samples.

Finally, the fitted function is integrated over the interval of θ_s [0,90]deg for the uniform samples to calculate the RMS roughness using the formula in Eq 4.4, using $n_{steel} = 2.5$ and $n_{air} = 1.00003$. For all the samples, the experimental data is integrated directly to calculate the scattered optical loss of the surface in the measurement interval [6,90]deg. All the results are shown in the following table.

Sample	TIS$_{th}$ from fit	TIS$_{exp}$ $(6 < \theta_s < 90$ deg)	$\sigma_{\lambda,th}$ (m) from fit
68B-u	$(122 \pm 39) \cdot 10^{-6}$	$106 \cdot 10^{-6}$	$(1.3 \pm 0.4) \cdot 10^{-9}$
69B-u	$(175 \pm 53) \cdot 10^{-6}$	$133 \cdot 10^{-6}$	$(1.5 \pm 0.5) \cdot 10^{-9}$
68B-nu	–	$240 \cdot 10^{-6}$	–
69B-nu	–	$1601 \cdot 10^{-6}$	–

Table 4.2: Estimation of the TIS for the samples. TIS$_{th}$ from simulated GHS model for the uniform baffle samples and TIS$_{exp}$ from experimental data for all the surfaces tested.

In conclusion, the "uniform" surfaces of the samples can be accurately represented by the GHS model, with consistent fit parameters across the two surfaces, resulting in similar values for TIS and RMS roughness. Notably, the TIS derived from experimental data is slightly underestimated compared to that obtained from the fit, consistent with the explanation provided in Sec. 4.1.1. This consistency between theory and measurements for smooth polished surfaces suggests that it is reasonably feasible to predict TIS from roughness or vice versa. However, the "non-uniform" surfaces require further investigation to provide a more comprehensive understanding of their scattering behavior.

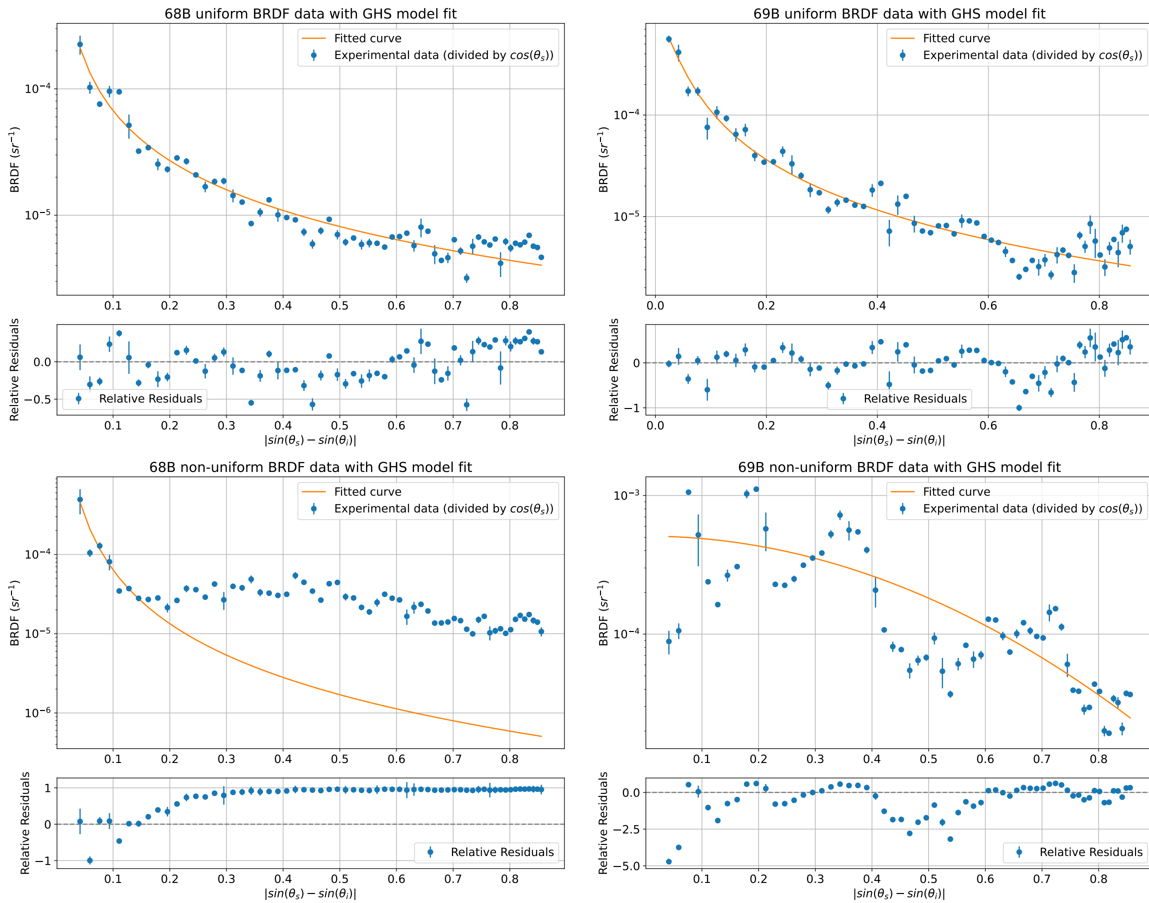

Figure 4.4: Plots of the BRDF of the baffle samples with the fit of the GHS model.

4.1.4 Absorbent glass samples

The EQB1 squeezing bench is part of an optical setup within the Virgo gravitational wave detector designed to produce and inject squeezed light into the detector, thereby reducing quantum noise and enhancing the detector's sensitivity to gravitational waves. To mitigate scattered light on EQB1 a number of stray light dumpers are displaced: they are made of absorbent glass slabs with AR coating. Samples of this material were sent to our laboratory for characterization using the scatterometer. These samples arrived already divided into two sets, but all absorbent glass samples are expected to have identical characteristics. Each sample is double-sided, with each surface being identical. We randomly selected two samples, one from each set, and measured the scattering for each side, denoting them as "G1-S1," "G1-S2," "G2-S1," and "G2-S2."

As with other samples, the 1064nm laser line was used, and also because this is one of the two laser lines circulating on EQB1. To prevent saturation, the filter with an OD of 2.81 was used for most of the measurement range, up to $\theta_s = 75deg$, with the minimum measurement angle of θ_s set at 6 degrees. The plot of the measured data is shown in Fig. 4.5. It is immediately noticeable that the G2-S1 sample exhibits significantly higher scattered light compared to the other three surfaces.

The GHS model fits were applied to the experimental data, shown in Fig. 4.6,

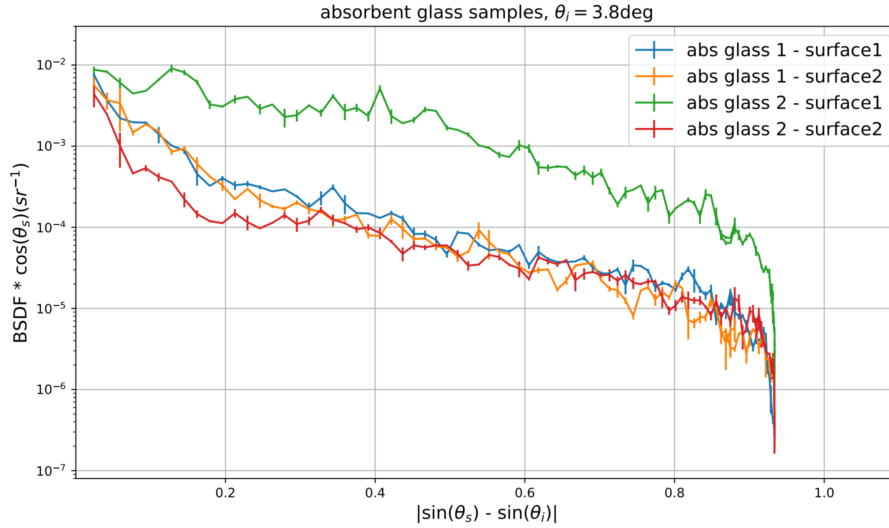

Figure 4.5: Plot of measured BRDF $\cdot$ $cos(\theta_s)$ data of the absorbent glass samples as a function of $|sin(\theta_s) - sin(\theta_i)|$.

yielding overall good agreement with the measurements for both surfaces of G1. However, the results from the G2-S1 data should be interpreted with caution, given the significant difference in scattered light compared to the other tested surfaces and the noticeable deviation of the data from the fit. Due to the small impinged area from the laser spot (about $1mm^2$), the anomalous scattering could have originated from a minor scratch or contaminant on the surface probed by the laser. For G2-S2, the fit seemed acceptable; however, the high error associated with the first point near specular reflection has made the estimation of the fit parameters b_0 and l unreliable, while the estimate for parameter s, dependent on large scattering angles, remained reliable. The fit parameters are presented in Table 4.6. Excluding the ones from the G2-S1 fit, as well as the b_0 and l for G2-S2, the parameters obtained are consistent with each other, particularly for the s parameter, with even the one obtained from the G2-S2 sample matches with the ones obtained from the G1 surfaces.

Sample	b_0 (sr^{-1})	l	s
G1-S1	$(144 \pm 12) \cdot 10^{-5}$	$(47 \pm 6) \cdot 10^{-3}$	-1.64 ± 0.08
G1-S2	$(156 \pm 18) \cdot 10^{-5}$	$(43 \pm 6) \cdot 10^{-3}$	-1.68 ± 0.11
G2-S1	$(81 \pm 6) \cdot 10^{-5}$	$(65 \pm 35) \cdot 10^{-2}$	-4.5 ± 3.5
G2-S2	0.3 ± 10^{5}	$10^{-4} \pm 3$	-1.82 ± 0.18

Table 4.3: Results of the parameters b_0, l and s of the GHS fit on the absorbent glass samples.

The BRDF was integrated to obtain the RMS roughness for the surfaces of the G1 sample and to calculate the optical loss in the measurement interval for the G2 sample. All results are shown in Table 4.4. To calculate Δn we use $n_{glass} = 1.5$ and $n_{air} = 1.00003$.

In conclusion, the G1 sample can be accurately characterized by the GHS model for surface scattering. However, further investigation is needed to identify a more

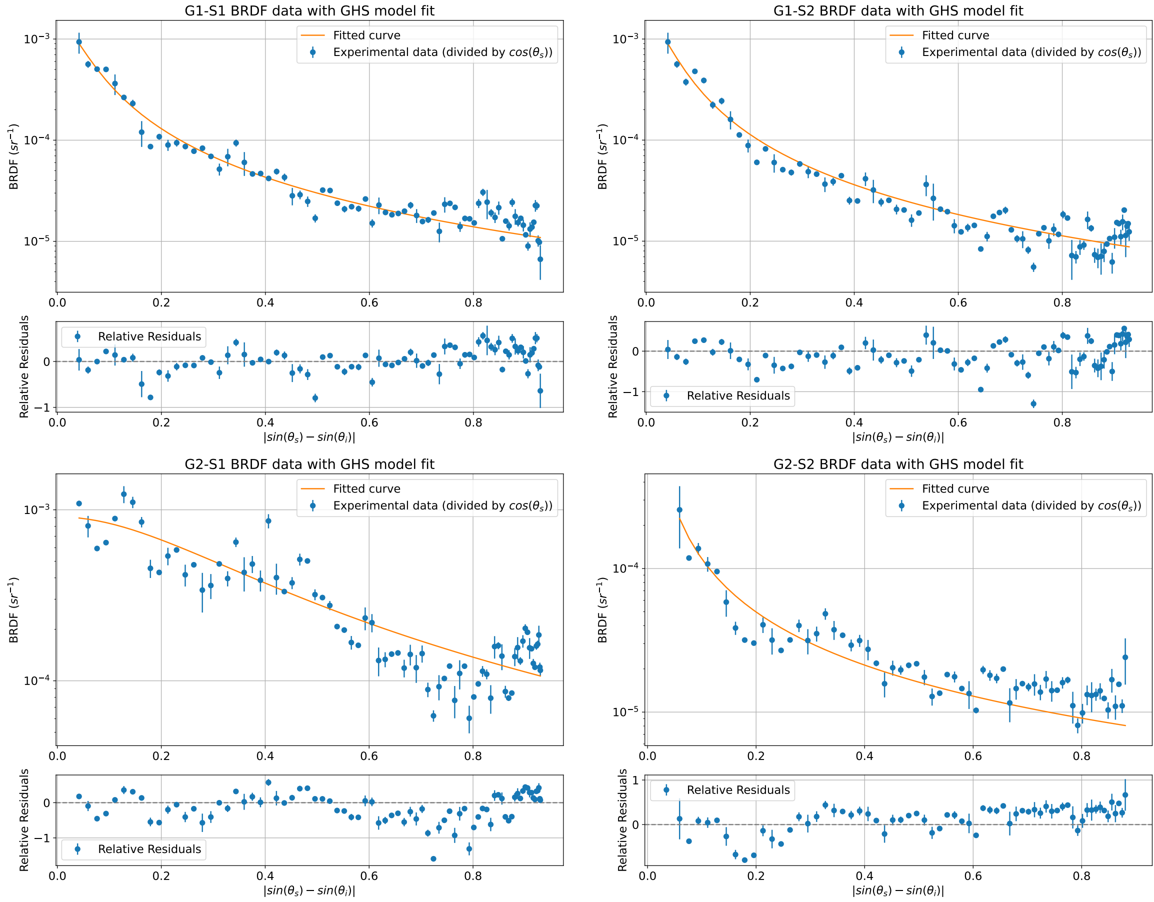

Figure 4.6: Plots of the BRDF of the absorbent glass samples with the fit of the GHS model.

Sample	TIS_{th} from fit	TIS_{exp} $(6 < \theta_s < 90$ deg$)$	$\sigma_{\lambda,th}$ (m) from fit
G1-S1	$(649 \pm 123) \cdot 10^{-6}$	$537 \cdot 10^{-6}$	$(8.7 \pm 1.6) \cdot 10^{-9}$
G1-S2	$(600 \pm 141) \cdot 10^{-6}$	$465 \cdot 10^{-6}$	$(8.3 \pm 1.9) \cdot 10^{-9}$
G2-S1	$(2600 \pm 2300) \cdot 10^{-6}$	$5090 \cdot 10^{-6}$	$(17 \pm 15) \cdot 10^{-9}$
G2-S2	–	$274 \cdot 10^{-6}$	–

Table 4.4: Estimation of the TIS for the samples. TIS_{th} from simulated GHS model for the uniform baffle samples and TIS_{exp} from experimental data for all the surfaces tested.

suitable model or understand the sources of variability in the G2-S1 sample data. Also, due to the unreliability of the parameters b_0 and l from the fit, new measurements should be conducted on the G2-S2 sample to confirm the modelization of the surface using the GHS model.

4.1.5 Clean Silicon wafer

The last type of samples studied for surface roughness are Silicon (Si) wafers used in the VIRGO laboratories to monitor dust deposition in areas where gravitational wave detectors operate. To estimate the stray light due to dust particulates on the

optics of GW detectors and the associated noise in GW measurements, a monitoring campaign of dust contamination in the Virgo Quantum Noise Reduction and other clean environments has been initiated in collaboration with the Virgo groups in Padova [26] (including the research group where I performed the internship). The goal of this campaign is to monitor contamination levels over time to understand how, where, and when dust accumulates most rapidly. For the monitoring campaign, clean 3-inch Si wafers are used as witness samples and are left exposed in the tested environments for a given period. They are then analyzed to measure and count the dust particles deposited, from which their distribution and expected BRDF are estimated. Subsequently, the same witness sample is analyzed with the scatterometer to compare the estimated BRDF from the particle count with the directly measured BRDF. Therefore, understanding the scattering properties of the witness sample where the dust is deposited is important.

In this section, I will analyze the scattering data from clean Si wafers to study the BRDF from surface roughness. In the next section, I will review the first data taken from the scattering of dust deposited on the same type of Si wafers. We have two types of Si wafers at our disposal: single-side polished (SSP) wafers, with the sample tested identified as "VU-10222," and double-side polished (DSP) wafers, with the sample tested identified as "SN-18423." The characterization of the samples is done on both surfaces, with the DSP wafer having two polished sides, and the SSP wafer having one polished side and one rough side. The residual roughness of the polished surfaces is about 0.6 nm, as stated by the manufacturer.

Due to the transparency of Si at the wavelength of 1064 nm, scattering can be measured both in the backward and forward directions. We measured with the DSP wafer, that about a third of the incident power of the laser is directly transmitted through the wafer. In addition, it must be noted that both the front and back surfaces will always contribute to the total measured scattering since the power reaching the back surface is a considerable fraction of the one hitting the front one. Measurements are conducted from θ_s of 5 degrees to 179 degrees, with θ_i set at 3.8 degrees. The measured BRDF $\cdot\, cos(\theta_s)$ is shown in Fig. 4.7. When comparing the reflected scattering between the DSP and SSP, it is evident that the reflected scattering of the SSP is dominated by the rough surface, even when the polished side is illuminated by the laser. This is due to the high transmissivity of the material combined with the very low thickness of the wafer, so the light passes through the wafer and encounters the rough side, thus being scattered. It is expected that the reflected scatter of the DSP is also contaminated by the scatter from the back surface, making the 1064 nm laser less suitable for studying the roughness of samples made from this material.

The measured BSDFs of the DSP wafer surfaces are consistent with each other, with the small differences attributed to the different areas probed by the laser.

The analysis of rough and polished surfaces for the SSP wafer presents a more complex scenario. The plot shows that the BRDF of the rough side is approximately two orders of magnitude higher than that of the polished side. However, the transmitted scattered light for both surfaces converges at angles $\theta_s > 140$ deg. Further investigations are required to understand the scattering behavior of SSP wafers under a 1064 nm incident laser.

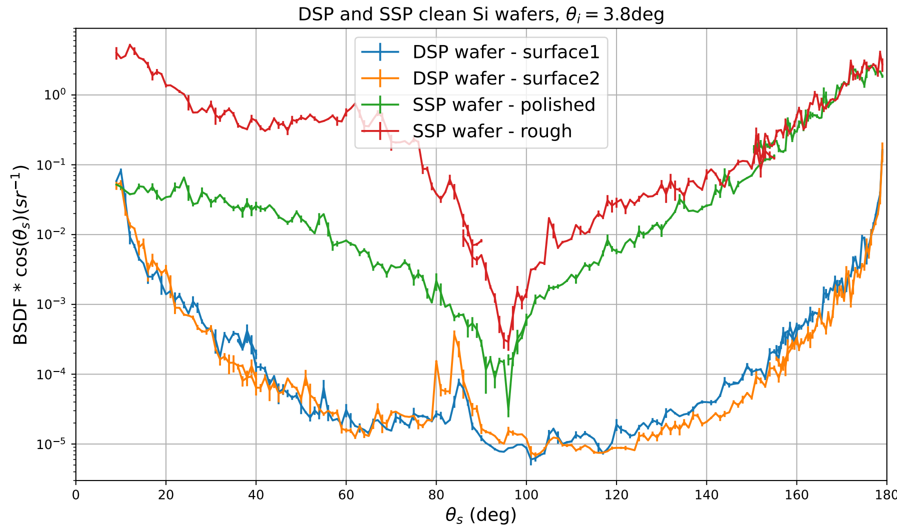

Figure 4.7: Plot of measured BRDF $\cdot$ $cos(\theta_s)$ data of the clean Si wafers as a function of θ_s using the 1064nm laser source.

With the 532 nm laser line now operational, we used this laser source to study the wafers. At this wavelength, the transparency of Si is negligible. In this case, the study is restricted to the SSP VU-10222 wafer, with two measurements conducted on the polished surface: one with a smaller laser spot and one with a larger laser spot, achieved by moving the L3 lens of the telescope. With L3 at a reference position of 15cm, the laser spot at the sample is about 1.5mm, while with L3 at 30cm, the laser spot is about 0.5mm. The measured data are shown in Fig. 4.8. Apart from a feature around $|sin(\theta_s) - sin(\theta_i)| \sim 0.9$ deg, the two measurements are consistent, and differences can be attributed to the different areas probed by the laser.

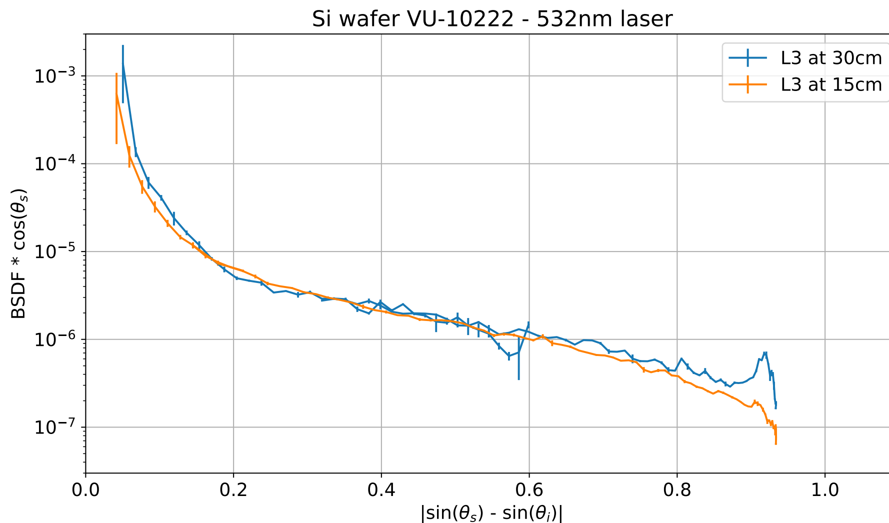

Figure 4.8: Plot of measured BRDF $\cdot$ $cos(\theta_s)$ data of the clean Si wafer VU-10222 as a function of $|sin(\theta_s) - sin(\theta_i)|$ using the 532nm laser source.

The measured data are then fitted with the GHS model, with the results shown in Fig . 4.9. However, the fitted curves do not represent the behavior of the data

sets. One possible explanation is due to the manufacturing process used to polish the wafer surfaces. Although the GHS model is valid for representing scattering from roughness, different polishing processes result in different power spectral density S_2 functions, making the GHS Eq. 2.46 derived with the K-correlation model used for the other samples invalid in this case.

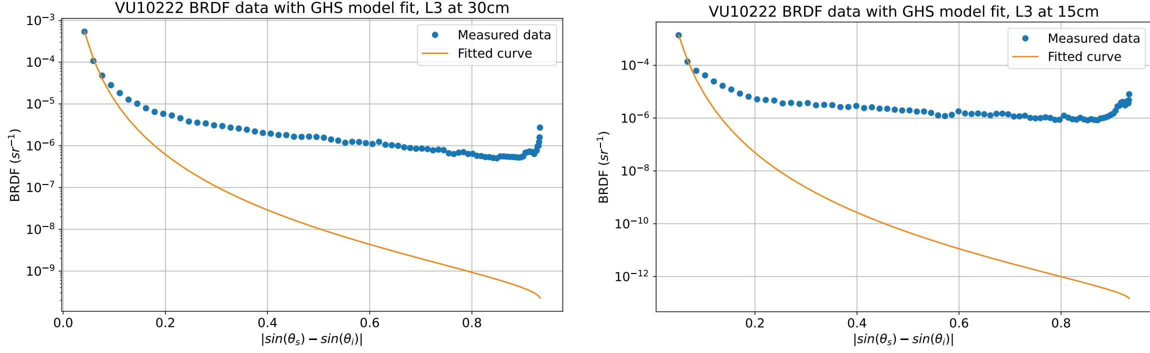

Figure 4.9: Plots of the BRDF of the Si wafer VU10222 with the fit of the GHS model.

Despite this, the isotropy of the surfaces allows for the calculation of scatter loss and, consequently, the lower limit of the RMS roughness in the measurement interval. The values obtained are presented in Table 4.5.

L3 position	TIS_{exp} $(6 < \theta_s < 90$ deg$)$	$\sigma_{\lambda,exp}\ (m)$
15cm	$42.4 \cdot 10^{-6}$	$1.85 \cdot 10^{-10}$
30cm	$24.7 \cdot 10^{-6}$	$1.40 \cdot 10^{-10}$

Table 4.5: Estimation of the TIS_{exp} from experimental data for the measurement done to the tested surface.

The RMS roughness value provided by the wafer producer is about 0.6 nm, and the lower limit obtained from our measurements is consistent with this value.

4.2 Dust scattering measurements

As for the sample roughness measurements, the same procedure for taking BRDF measurements is followed. The samples studied are the same type of Si wafer whose clean BRDF was measured in the previous section. However, in this case, the Si wafers are contaminated with calibrated dust, consisting of known materials with specific characteristics. After measuring the BRDF of a sample with the scatterometer, the same spot where the laser impinged the contaminated wafer is analyzed with a digital microscope, model Keyence VHX-7000. Photos are taken at different scales, and the microscope software analyzes the images, counting the contaminants while measuring various related quantities, such as diameter.

A Python script, written is used to divide the particles into intervals of diameter D_i, and the particle size distribution function $f(D_i)$ is computed. Using functions from the miepython library, based on the Mie scattering model reviewed in Sec.

2.3, it is possible to simulate the BRDF from the $f(D_i)$ function measured with the digital microscope and the physical characteristics of the dust and Si wafer.

The ones discussed here are the first preliminary measurements performed on samples contaminated with dust using our scatterometer. The calibrated dust serves as a reference for the measurement procedure that will later be conducted on Si wafers contaminated by dust deposited in the VIRGO laboratories.

4.2.1 Wafer contaminated by Ti calibrated dust

The calibrated dust used to artificially contaminate the wafer is made of Titanium (Ti). The contamination on the wafer is not uniform, presenting areas with varying densities of particulates. Therefore, two measurements are taken with the scatterometer: one where the laser impinges at the center of the wafer, labeled as "center," and one where the laser impinges on an area with visibly higher particulate density, labeled as "pos2."

As with the clean wafer, the 532 nm laser line was used at an incidence angle of $\theta_i = 3.8$ degrees. The L3 lens is set to 15 cm to produce a larger beam spot, allowing for a better average density measurement of the contaminants (spot area $\sim 2mm^2$). The plot of the measured data is shown in Fig. 4.10. As expected, the scattering from dust in the "pos2" position is higher compared to the center position.

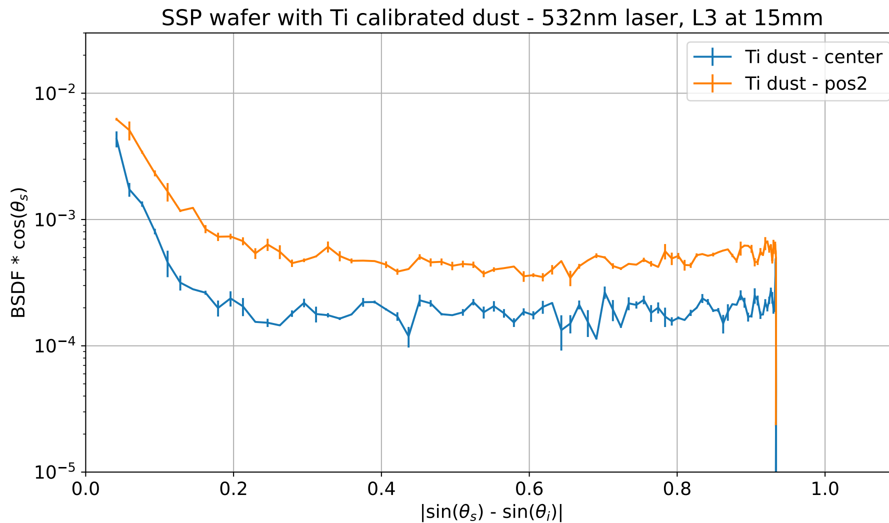

Figure 4.10: Plot of measured BRDF $\cdot\, cos(\theta_s)$ data of the Si wafer contaminated by Ti calibrated dust as a function of $|sin(\theta_s) - sin(\theta_i)|$ using the 532nm laser source.

The wafer is then analyzed with a digital microscope to take images of the two different spots probed by the laser. To align the microscope with the same areas, photos were taken of the wafer illuminated by the laser while it was still in the scatterometer. These reference photos were used to manually center the microscope on the wafer spots. Photos were taken at magnifications of x20, x50, and x100, with corresponding areas of $169mm^2$, $25mm^2$, and $6mm^2$, respectively. With this procedure, we expect that the laser spot is captured at least in the x20 magnification photo. Each photo is processed by the microscope software, and then the Python script computes $f(D_i)$ and the respective BRDF.

As can be noted in Fig. 4.11, the variation of the distribution of the contaminants along the area is noticeable also at the magnification of x20. It is important to note that the area probed by the laser spot ($2mm^2$), has a similar area only to the dimensions of the photo at magnification x100 ($6mm^2$). While the estimations from the photos at smaller magnifications yield values averaged in the significantly larger areas, the estimation from the photo at x100 can have higher fluctuation depending on where the photo is taken, and the reliability of the values depends on the precision alignment with the microscope.

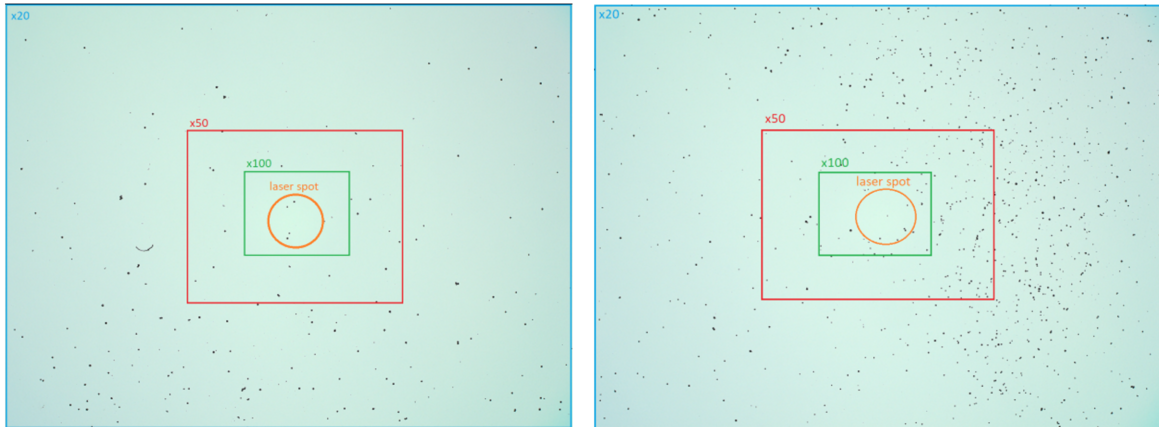

Figure 4.11: Photos taken with the digital microscope at the wafer contaminated with Ti dust (left is "center", right is "pos2") used for estimating the BRDFs. The positions of the sketched laser spots in the images represent the guessed position impinged by the laser. For reference, the width of the photos at x20, x50, and x100 are respectively 15mm, 6mm, and 3mm. The diameter of the laser spot is 1.5mm.

Fig. 4.12 shows the comparisons between the measured BRDF $\cdot\, cos(\theta_s)$ data and the simulated values. The measured data for both the center and pos2 positions are slightly higher than the simulated values estimated with the x100 magnification photo. While the accuracy of the estimation with the latter magnification is not optimal, it gives information on the order of magnitude of the scattered light.

The BRDF values estimated from the other photos at higher magnification are less consistent with the measured data. This discrepancy is likely due to a mismatch between the area imaged by the microscope with respect to the area probed by the laser spot of the scatterometer. The area probed by the laser is only a few mm^2, making it easy to miss when aligning by eye. This is evident in Fig. 4.11, where the position of the x100 magnification photo is taken can heavily impact the estimation of $f(D_i)$, also by changing its position by a few millimeters.

In conclusion, the discrepancy between the measured data and the simulated values needs further investigation. One possible explanation could be inaccuracies in the procedure for photographing the laser-impinged spots. This is the first time the scatterometer has been used in combination with the digital microscope, and the procedure is still rudimentary and requires improvements.

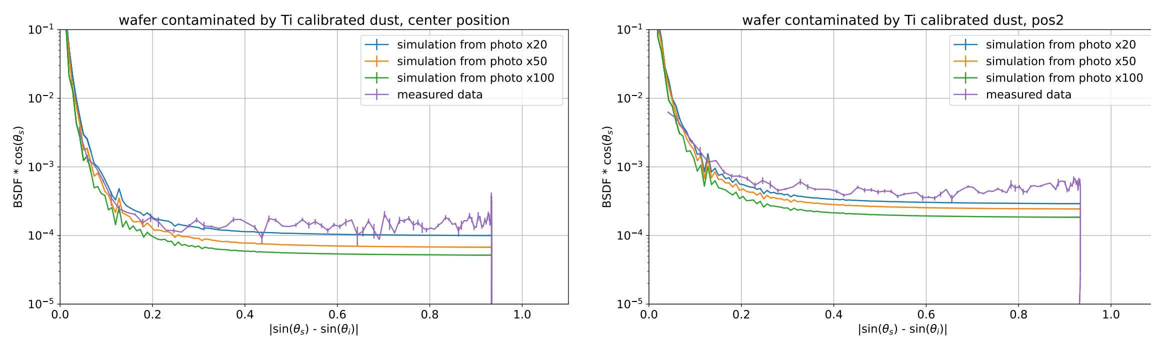

Figure 4.12: Plots of the comparison between the measured BRDF $\cdot$ $cos(\theta_s)$ of the contaminated Si wafer with the simulation by the Mie scattering model.

Chapter 5

Conclusion

Stray light presents a significant challenge as it manifests as excess noise in the low-frequency region of the current LIGO-VIRGO interferometers, causing a loss in sensitivity both through excess noise in measurements and by disrupting control loops. This issue is expected to be even more critical in the next generation of interferometers, such as the Einstein Telescope (ET), which is designed to have higher sensitivity in the low-frequency region. Therefore, it is essential to understand and mitigate stray light sources effectively.

Among the primary contributors to stray light are the surface roughness of the optics and the scattered light from dust particles deposited on the optics. Notably, due to the very low surface roughness of the optics, estimations have shown that dust contributions to stray light can surpass the effects caused by surface roughness, even in clean environments. This underscores the importance of understanding and controlling dust contamination to maintain the high sensitivity of gravitational wave detectors.

To model and characterize the sources of stray light, two important quantities are utilized: the Bidirectional Scattering Distribution Function (BSDF), which describes the angular distribution of light scattered from a surface, and the Total Integrated Scattering (TIS), which measures the total scattered light over all angles within a hemisphere. In this thesis, the principal models used to characterize scattering from surface roughness and particulates were reviewed. The Harvey-Shack model, a parametrization of the Rayleigh-Rice perturbation theory, establishes a direct relationship between the BSDF and the PSD of surface roughness. The more general Generalized Harvey-Shack (GHS) model extends the capabilities of the original Harvey-Shack model by accommodating larger scattering and incidence angles and accounting for both smooth and rough surfaces. This versatility allows for a more accurate representation of real-world scattering phenomena. In combination with the K-Correlation model, it effectively describes the PSD of polished surfaces and provides a comprehensive description of surface roughness and its impact on scattering.

Additionally, Mie scattering theory addresses the scattering of light by particles that are comparable in size to the wavelength of the light. This type of scattering is crucial for understanding how dust and other particulate contaminants affect the optical performance of detectors.

The research group of DFA and INFN, based in Padua, in collaboration with VIRGO, has made significant efforts in building a scattering measurement facility to directly measure the BSDF and TIS of samples. My work commenced with the facility already operational but not at its optimal status. Part of my work focused on enhancing the optical setup. One of the key improvements was the optimization of the background noise of the scatterometer, an instrument that is part of the facility and is used to measure the BSDF on target samples. This involved identifying and mitigating sources of stray light within the instrument. Initial background measurements revealed significant noise, which was traced back to various internal reflections and scattering from optical and mechanical components. By strategically adding irises and masking critical parts of the setup, these stray light sources were effectively minimized, enabling high-precision BRDF measurements close to the ultimate limit imposed by Rayleigh scattering of the air molecules.

Other improvements, such as the installation of the pick-up detector and the motorized HWP, aimed at automating the measurement procedure for characterizing sample scattering, that, with the help of custom software to operate the instrument, will significantly reduce the time needed to characterize each sample.

With the optimized instrument, I conducted a measurement campaign of various samples. While the BSDF by itself is a useful quantity, using the models derived in the thesis, it can be used to characterize the sample by predicting the behavior of the BSDF at different angles and obtaining important quantities such as surface roughness. For this purpose, different samples, some of which were sourced from other laboratories, were characterized by their scattering from roughness.

The measurements of baffle samples from VIRGO detectors indicated distinct scattering behaviors between the "uniform" and "non-uniform" surfaces, with the latter showing higher scattering and variability. The application of the GHS model provided a good fit for the uniform surfaces, while the non-uniform surfaces show anomalous behavior and require further exploration.

The absorbent glass samples for the EQB1 squeezing bench revealed significant differences in scattering between the two sets of samples studied. While the GHS model fit well for some surfaces, others, like G2-S1, showed substantial variability, indicating the need for further investigation to understand the sources of scatter.

The silicon wafers used in the dust monitoring campaign highlighted the challenges posed by high transparency at certain wavelengths. While the 1064 nm laser proved inadequate due to excessive transparency, the 532 nm laser provided better results. The scattering data from clean wafers were used to estimate a lower bound for the effective roughness, with values consistent with the manufacturer's specifications.

Finally, the analysis of Si wafers contaminated with calibrated dust provided insights into the scattering behavior of dust particles. The combination of scatterometer measurements and digital microscopy allowed for a detailed examination of particle distributions and their impact on scattering. However, discrepancies between measured and simulated data underscored the need for improved procedures in aligning the microscope with the laser-impinged spots.

Part of the failed modeling of the samples arises from the low statistics of the measurements taken. Each measurement takes considerable time, making it difficult

to perform multiple measurements on the same samples. In the future, with the automation of the measurement procedure, this will no longer pose a problem. In cases of atypical or unexpected behavior in the measured data, it will be easier to take additional measurements to understand if a sample exhibits different behavior or if eventually, the area probed by the laser presented unexpected features, like scratches on the surface.

Regarding the future prospects of the scattering measurement facility, several important improvements still need to be made. Specifically, the integrating sphere needs to be repositioned to its proper location. This adjustment will also enable the implementation of optical elements for the 1550 nm laser line, making it operational. In the meantime, the measurement focus will remain on the objectives of the dust monitoring campaign. New wafers will be periodically exposed in different environments of the VIRGO laboratories to continue monitoring dust accumulation and increase the statistical data, both through repeated measurements and over time. Additionally, a more accurate monitoring of specific human activities, such as commissioning operations, will be performed to assess their impact on dust deposition. The BSDF of these Si wafers will be experimentally measured using our scattering measurement facility to determine if the experimental results align with the BSDF estimates computed from the measured dust distribution.

Bibliography

[1] M. Maggiore, *Gravitational Waves. Vol. 1: Theory and Experiments.* Oxford University Press, 2007.

[2] Éanna É Flanagan and S. A. Hughes, "The basics of gravitational wave theory," *New Journal of Physics*, vol. 7, no. 1, p. 204, sep 2005. [Online]. Available: https://dx.doi.org/10.1088/1367-2630/7/1/204

[3] L. Ju, D. Blair, and C. Zhao, "Detection of gravitational waves," *Reports on Progress in Physics*, vol. 63, p. 1317, 08 2000.

[4] F. Acernese, "Status of advanced virgo," *EPJ Web Conf.*, vol. 182, p. 02003, 2018. [Online]. Available: https://doi.org/10.1051/epjconf/201818202003

[5] R. Abbott, "Gwtc-3: Compact binary coalescences observed by ligo and virgo during the second part of the third observing run," *Physical Review X*, vol. 13, no. 4, Dec. 2023. [Online]. Available: http://dx.doi.org/10.1103/PhysRevX.13.041039

[6] T. L. S. Collaboration and V. Collaboration, "GWTC-3: Compact Binary Coalescences Observed by LIGO and Virgo During the Second Part of the Third Observing Run," *arXiv e-prints*, Nov. 2021. [Online]. Available: https://arxiv.org/abs/2111.03606

[7] M. Punturo *et al.*, "The Einstein Telescope: A third-generation gravitational wave observatory," *Class. Quant. Grav.*, vol. 27, p. 194002, 2010.

[8] *Third Generation Gravitational Wave detectors: the challenge of Einstein Telescope in Europe.* Zenodo, Apr. 2020. [Online]. Available: https://doi.org/10.5281/zenodo.3567575

[9] E. Thrane and C. Talbot, "An introduction to bayesian inference in gravitational-wave astronomy: Parameter estimation, model selection, and hierarchical models," *Publications of the Astronomical Society of Australia*, vol. 36, 2019. [Online]. Available: http://dx.doi.org/10.1017/pasa.2019.2

[10] B. P. Abbott, "Observation of gravitational waves from a binary black hole merger," *Phys. Rev. Lett.*, vol. 116, p. 061102, Feb 2016. [Online]. Available: https://link.aps.org/doi/10.1103/PhysRevLett.116.061102

[11] B. Abbott, "Observation of gravitational waves from a binary black hole merger," *Physical Review Letters*, vol. 116, no. 6, Feb. 2016. [Online]. Available: http://dx.doi.org/10.1103/PhysRevLett.116.061102

[12] J. Marque and G. Vajente, *Stray Light Issues.* Cham: Springer International Publishing, 2014, pp. 275–290. [Online]. Available: https://doi.org/10.1007/978-3-319-03792-9_10

[13] W. Jarosz, V. Schönefeld, L. Kobbelt, and H. W. Jensen, "Theory, analysis and applications of 2d global illumination," *ACM Transactions on Graphics (Presented at SIGGRAPH)*, vol. 31, no. 5, pp. 125:1–125:21, Sep. 2012.

[14] E. Fest, *Stray Light Analysis and Control.* Bellingham, Washington: SPIE Press, 2007.

[15] Wikipedia, "Bidirectional scattering function," https://en.wikipedia.org/wiki/Bidirectional_scattering_distribution_function, 2023.

[16] A. Krywonos, J. E. Harvey, and N. Choi, "Linear systems formulation of scattering theory for rough surfaces with arbitrary incident and scattering angles," *J. Opt. Soc. Am. A*, vol. 28, no. 6, pp. 1121–1138, Jun 2011. [Online]. Available: https://opg.optica.org/josaa/abstract.cfm?URI=josaa-28-6-1121

[17] J. Harvey and R. Pfisterer, "Comparison of the ghs smooth and the rayleigh-rice surface scatter theories," 09 2016, p. 996103.

[18] P. R. Spyak and W. L. Wolfe, "Scatter from particulate-contaminated mirrors. part 2: theory and experiment for dust and lambda;=0.6328 mu;m," *Optical Engineering*, vol. 31, no. 8, pp. 1757 – 1763, 1992. [Online]. Available: https://doi.org/10.1117/12.58709

[19] G. Mie, "Contributions to the optics of turbid media, particularly of colloidal metal solutions," *Annalen der Physik*, vol. 330, no. 3, pp. 377–445, 1908. [Online]. Available: https://onlinelibrary.wiley.com/doi/abs/10.1002/andp.19083300302

[20] M. H. Brill, "Seeing the light: Optics in nature, photography, color, vision, and holography, by david s. falk, dieter r. brill, and david g. stork, harper and row, new york, 1986, 446 pp. price: $35.50," *Color Research & Application*, vol. 12, no. 3, pp. 156–157, 1987. [Online]. Available: https://onlinelibrary.wiley.com/doi/abs/10.1002/col.5080120310

[21] L. Hu, F. Jiang, and C. Chen, Eds., *Emerging Nanotechnologies in Nanocellulose*, ser. NanoScience and Technology. Springer Cham, 2022, published: 01 November 2022.

[22] I. T. Schmiegelow, "Characterizing light scattering sources in gravitational-wave interferometers," Master's Degree in Astrophysics and Cosmology, Università degli Studi di Padova, Dipartimento di Fisica e Astronomia "Galileo Galilei", Padova, Italy, 2023, thesis supervisor: Prof. Giacomo Ciani, Thesis co-supervisors: Dr. Livia Conti, Dr. Giulio Favaro.

[23] C. Asmail, J. Hsia, A. Parr, and J. Hoeft, "Rayleigh scattering limits for low-level bidirectional reflectance distribution function measurements," *Appl. Opt.*, vol. 33, no. 25, pp. 6084–6091, Sep 1994. [Online]. Available: https://opg.optica.org/ao/abstract.cfm?URI=ao-33-25-6084

[24] C. Asmail, A. Parr, and J. Hsia, "Rayleigh scattering limits for low-level bidirectional reflectance distribution function measurements: Corrigendum," *Applied optics*, vol. 38, pp. 6027–8, 11 1999.

[25] A. Moscatello, G. Favaro, G. Ciani, and L. Conti, "Tis and roughness measurements on samples of stainless steel from cern," *ET TDS Code: ET-0335A-23*, October 2023.

[26] A. Moscatello, "Light scattering from dust contamination in gravitational-wave interferometric detectors," Master's thesis, Università degli Studi di Padova, Dipartimento di Fisica e Astronomia "Galileo Galilei", Padova, Italy, June 2022, master Degree in Physics, Thesis supervisor: Prof. Giacomo Ciani, Thesis co-supervisor: Dr. Livia Conti.